Journal of
Marine Science and Engineering

MDPI

Article

Transient Translational–Rotational Motion of an Ocean Current Converter Mooring System with Initial Conditions

Shueei-Muh Lin *, Wen-Rong Wang and Hsin Yuan

Green Energy Technology Research Centre (GETRC), Department of Mechanical Engineering, Kun Shan University, Tainan 710, Taiwan; me70ks10@mail.ksu.edu.tw (W.-R.W.); qeye@yahoo.com.tw (H.Y.)
* Correspondence: smlin@mail.ksu.edu.tw

Abstract: Systems of ocean current power generation are generally moored deep in the seabed. The mooring system is like ropes. The ropes are very long and can provide tension but not compression, and their dynamic displacement is large and unstable, which is different from traditional structures. To generate high-efficiency ocean current power generation, it is necessary to design a stable mooring system. Maintaining the stability and small dynamic displacement of the ocean current invertor is significantly helpful for the high efficiency of the invertor. In addition, the stability of the mooring system and a small dynamic tension, high safety factor, and long life of the mooring ropes are essential. In this study, we investigate the transient behavior of a mooring system composed of an inverter platform, pontoon, and ropes under initial conditions. An analytical method is proposed. The transient translational and rotational displacements are composed of 36 independent normalized fundamental solutions. The composition depends on the initial conditions. Each fundamental solution is derived by using the Frobenius method. This study proposes the replacement of the traditional single-rope mode with the double-rope parallel mode, which can maintain a high fracture strength and low effective spring constant in the rope. It is verified that this design can decrease instantaneous tension and increase the safety factor of the rope. Additionally, high hydrodynamic damping coefficients can significantly increase the stability of the mooring system.

Keywords: transient motion; initial condition; double-rope parallel mode; ocean current; mooring system; stability

Citation: Lin, S.-M.; Wang, W.-R.; Yuan, H. Transient Translational–Rotational Motion of an Ocean Current Converter Mooring System with Initial Conditions. *J. Mar. Sci. Eng.* **2023**, *11*, 1533. https://doi.org/10.3390/jmse11081533

Academic Editor: Unai Fernandez-Gamiz

Received: 14 June 2023
Revised: 14 July 2023
Accepted: 20 July 2023
Published: 31 July 2023

1. Introduction

Ocean current power generation is a potential renewable energy technology. Global ocean currents are rich in energy. The currents have a mean velocity of about 1.2~1.53 m/s near the surface. The Taiwan Kuroshio current has a potential capacity of over 4 GW [1]. In general, the seabed beneath the current is over 1000 m. Studies on deep mooring technology have helped to harness that energy [2]. The stability of ocean power generation systems under coupled typhoon wave currents must be investigated [3]. With respect to such systems, the development of an ocean current generator, the related design, and the development of mathematical models and analysis methods are important topics.

In terms of the practical testing of ocean current generators set in the sea, Chen et al. [1] successfully tested a 50 kW ocean current convertor moored to an 850 m deep seabed beneath the Taiwan Kuroshio current. At a current speed of 1.0 m/s, the output power of the system was 26 kW. IHI and NEDO [4] successfully tested a 100 kW convertor moored to a 100 m deep seabed beneath the Japan Kuroshio current. The current converter generated about 30 kW under the current speed of 1.0 m/s.

For mathematical models of the mooring systems for ocean current generation, Lin et al. [3] proposed a mathematical model of a coupled-surface invertor–platform–rope mooring system under regular waves and ocean currents. The dynamic stability of the in-plane motion of the mooring system, in four degrees of freedom, was investigated. It was found

that the effects of some parameters on the dynamical stability of the mooring system were significant. Lin and Chen [5] proposed the design of a submarine floating platform-towed parachute–pontoon–traction rope mooring system to prevent damage induced by typhoon waves. The dynamic stability of the in-plane motion of the mooring system possessed three degrees of freedom, and the concentrated mode was investigated. The stability and safety of the proposed design subjected to typhoon waves and currents was verified. Lin et al. [6] proposed the design of a submarine invertor-surfaced platform–pontoon–traction rope mooring system. The dynamic stability of the in-plane motion of the mooring system possessed five degrees of freedom, and the conditions of a concentrated mode under regular waves and a steady ocean current were investigated. The stability and safety of the proposed design subjected to typhoon waves and currents was verified. Only the hydrodynamic surge forces on the converter and the platform were considered. Lin et al. [7] presented the design of a submarine invertor–submarine platform–pontoon–traction rope mooring system to generate power from undergoing typhoon wave impact and currents. The dynamic stability of the in-plane translational motion of the mooring system possessed six degrees of freedom, and the concentrated mode under irregular waves and a steady ocean current was investigated. Irregular waves were simulated on the basis of several regular waves and were constructed using the Jonswap wave spectrum model. Meanwhile, only the hydrodynamic surge forces on the converter and platform were considered. Lin et al. [8] presented a mathematical model of the coupled translational–rotational motions of a mooring system for an ocean energy convertor with 18 degrees of freedom. The coupled fluid–structure interaction was investigated. The hydrodynamic forces and moments on the converter and the platform were determined using the computational fluid dynamic method. Furthermore, the hydrodynamic damping and stiffness parameters were obtained. However, the hydrodynamic damping of the two pontoons was neglected. All elements have traditionally been connected by a single rope. The spectral response and stability of the mooring system with the coupled fluid–structure parameters under the action of periodic waves were investigated.

The theory and technology of fluid–structure interactions (FSIs) have been widely applied in many different fields, including marine engineering [9], aerodynamics [10], acoustics [11], and medicine [12,13].

Anagnostopoulos [9] studied wave–offshore platform interaction. The hydrodynamic force was simulated using the Morison model.

Lin et al. [12,13] investigated the wave modes of an elastic tube conveying blood. An analytical solution for the system was presented. The authors discovered the flexural, Young, and Lamb modes. The energy transmission mechanisms of the three modes through the blood vessel and blood vessel interactions were studied.

Due to the complexity of the fluid–structure interactions, FSI problems are usually solved using numerical methods. Belibassakis [14] presented a hydrodynamic analysis of a floating body using the boundary element method. Tsui et al. [15] investigated fluid–elastic plate interactions using a finite-volume-based approach. Hasanpour et al. [16] studied wave–coastal structure interactions using the coupled SPH–FEM model.

There is no discussion in the literature [3,5–8] on the transient responses of mooring systems. Therefore, in this study, the transient motion, stability, and rope tension of the ocean current power generation mooring system [8] with initial conditions and hydrodynamic forces and moments are analyzed. This study could be of significant assistance in maintaining the high efficiency and long lifespan of ocean current power generation systems.

2. Mathematical Model

2.1. Dynamic Governing Equations

To avoid the wave impact of typhoons, the energy converter and the floating platform were submerged to a safe depth. Two small floating pontoons are connected to the convertor and the platform, respectively, using a rope, as shown in Figure 1. In the mooring system,

the converter is mounted below the surface of the water at some safe depth so that it will remain undamaged and stably generate electricity under wave impact. In this study, the mathematical model of the mooring system proposed by Lin et al. was adopted [8]. Furthermore, the transient response of this model was investigated after setting some initial conditions. The governing equation is in the matrix format, as follows:

$$\mathbf{M}\frac{d^2\mathbf{Z}_d}{dt^2} + \mathbf{C}\frac{d\mathbf{Z}_d}{dt} + \mathbf{K}\mathbf{Z}_d = 0 \tag{1}$$

where $\mathbf{Z}_d = \left[x_{1d}\ y_{1d}\ z_{1d}\ x_{2d}\ y_{2d}\ z_{2d}\ x_{3d}\ y_{3d}\ z_{3d}\ x_{4d}\ y_{4d}\ z_{4d}\ \varphi_{Tx}\ \varphi_{Ty}\ \varphi_{Tz}\ \varphi_{Px}\ \varphi_{Py}\ \varphi_{Pz}\right]^T$,

$$\mathbf{M} = \begin{bmatrix} M_{1,1} & 0 & \cdots & 0 \\ 0 & M_{2,2} & \cdots & 0 \\ \vdots & \vdots & \ddots & \vdots \\ 0 & 0 & \cdots & M_{n,n} \end{bmatrix}, \mathbf{C} = \begin{bmatrix} C_{1,1} & \cdots & C_{1,18} \\ \vdots & \ddots & \vdots \\ C_{18,1} & \cdots & C_{18,18} \end{bmatrix}, \mathbf{K}(t) = \begin{bmatrix} K_{1,1}(t) & \cdots & K_{1,18}(t) \\ \vdots & \ddots & \vdots \\ K_{18,1}(t) & \cdots & K_{18,18}(t) \end{bmatrix}. \tag{2}$$

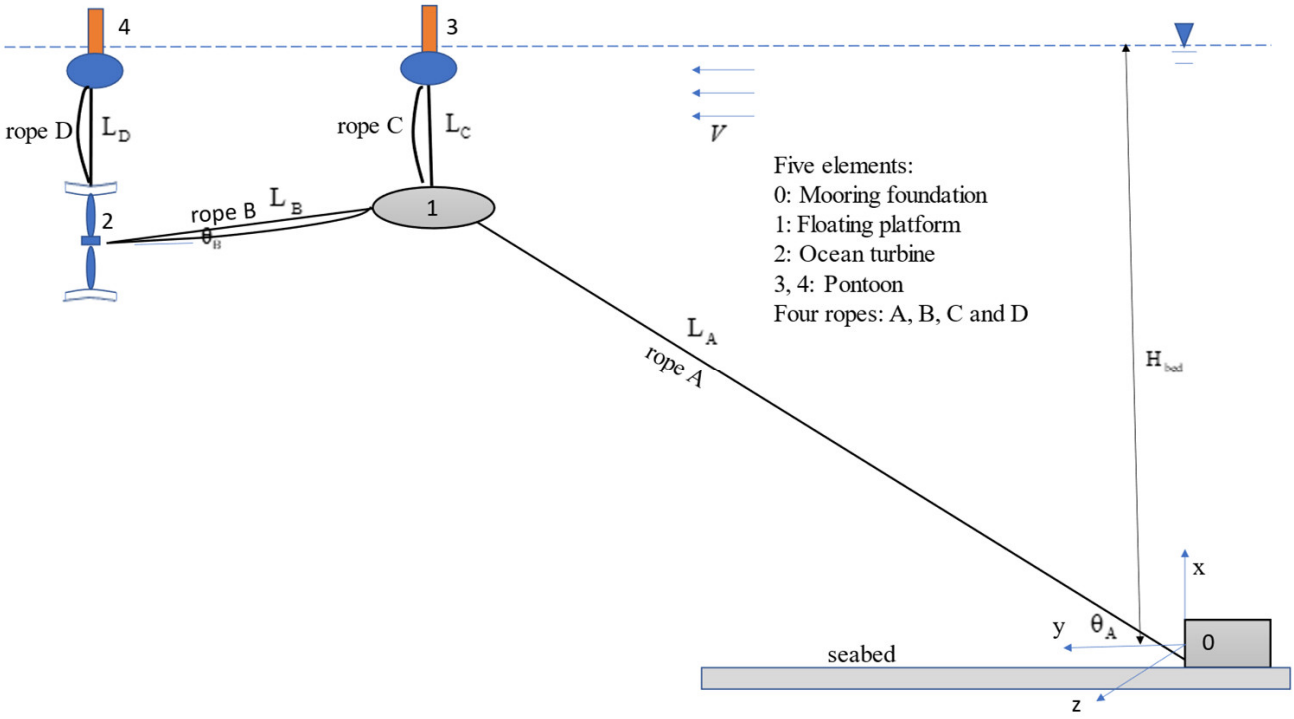

Figure 1. Configuration of the mooring system for the ocean energy convertor.

The elements of the mass, hydrodynamic damping, and stiffness matrices **M**, **C**, and **K** are listed in Appendix A, Appendix B, and Appendix C, respectively. Lin et al. [8] derived the hydrodynamic damping coefficients of the proposed inverter and platform. However, the hydrodynamic damping in pontoons 3 and 4 was neglected. In this study, the hydrodynamic heaving damping of pontoons 3 and 4 was considered, and the values are listed in Appendix B in order to clearly investigate the transient stability of the system. There are 36 initial conditions, as follows:

The initial translational and rotational displacements:

$$\mathbf{Z}_d(0) = \left[x_{1d0}\ y_{1d0}\ z_{1d0}\ x_{2d0}\ y_{2d0}\ z_{2d0}\ x_{3d0}\ y_{3d0}\ z_{3d0}\ x_{4d0}\ y_{4d0}\ z_{4d0}\ \varphi_{Tx0}\ \varphi_{Ty0}\ \varphi_{Tz0}\ \varphi_{Px0}\ \varphi_{Py0}\ \varphi_{Pz0}\right]^T \tag{3}$$

The initial translational and rotational velocities:

$$\frac{d\mathbf{Z}_d(0)}{dt} = \left[\dot{x}_{1d0}\ \dot{y}_{1d0}\ \dot{z}_{1d0}\ \dot{x}_{2d0}\ \dot{y}_{2d0}\ \dot{z}_{2d0}\ \dot{x}_{3d0}\ \dot{y}_{3d0}\ \dot{z}_{3d0}\ \dot{x}_{4d0}\ \dot{y}_{4d0}\ \dot{z}_{4d0}\ \dot{\varphi}_{Tx0}\ \dot{\varphi}_{Ty0}\ \dot{\varphi}_{Tz0}\ \dot{\varphi}_{Px0}\ \dot{\varphi}_{Py0}\ \dot{\varphi}_{Pz0}\right]^T \quad (4)$$

2.2. Integration of Two Ropes with Different Lengths in Parallel

The larger the effective spring constant K, the greater the tension caused by the momentary movement, because there is less elastic cushioning. The K value is inversely proportional to the length but is proportional to the diameter, and the breaking force is also proportional to the diameter. To reduce the tension generated by the rope, a smaller diameter can be used, but its breaking force may not be sufficient, so a multi-parallel multi-section K value design was adopted. When the first rope is broken, the other one is still safe, making the mooring system better protected. The overall fracture strength and the flexibility of the integrated rope are high.

For this deep mooring system, the main mooring rope A is very long, and its effective spring constant is small. Therefore, the buffering effect is significant. However, because the rope i, $i = B, C$, or D are too short, their effective spring constants are very large, and the buffering effect is very low. In this study, it is proposed that the rope i, where $I = B, C$, or D consists of the integration of two ropes, $i\alpha$ and $i\beta$, in parallel. The buffering effect of these integrated ropes is high, and their fracture strength is great.

2.2.1. Relation between Tension and Elongation

The lengths of ropes 1 and 2 without tension are $L_{i\alpha}$ and $L_{i\beta}$, where $L_{i\beta} > L_{i\alpha}$. The effective spring constants of the two ropes are $\overline{K}_{ij} = E_{ij}A_{ij}/L_{ij0}$, $i = B, C, D$; $j = \alpha, \beta$. When the elongation of the integrated rope $\delta_i < 0$, in stage 0, its tension is zero, i.e., the integrated effective spring constant $K_i = K_{i0} = 0$. When the elongation of the integrated rope is in the interval $0 < \delta_i < L_{i\beta} - L_{i\alpha}$ in stage 1, the integrated effective spring constant is $K_i = K_{i1} = \overline{K}_{i\alpha}$. When the elongation of the integrated rope δ_i is greater than the critical one $\delta_{ic1} = L_{i\beta} - L_{i\alpha}$, in stage 2, the integrated effective spring constant is $K_i = K_{i2} = \overline{K}_{i\alpha} + \overline{K}_{i\beta}$, as shown in Figure 2. The critical tension was $\overline{T}_{ic} = \overline{K}_{i\alpha}(\delta_{ic1} + \delta_{i\beta})$, which is lower than the fracture strength of rope $i\alpha$. The effective spring constant of rope i is

$$K_i = \begin{cases} 0, & \delta_i \le 0 \\ \overline{K}_{i\alpha}, & 0 \le \delta_i \le \delta_{ic1}, \\ \overline{K}_{i\alpha} + \overline{K}_{i\beta}, & \delta_{ic1} \le \delta_i \end{cases} \quad i = B, C, D \quad (5)$$

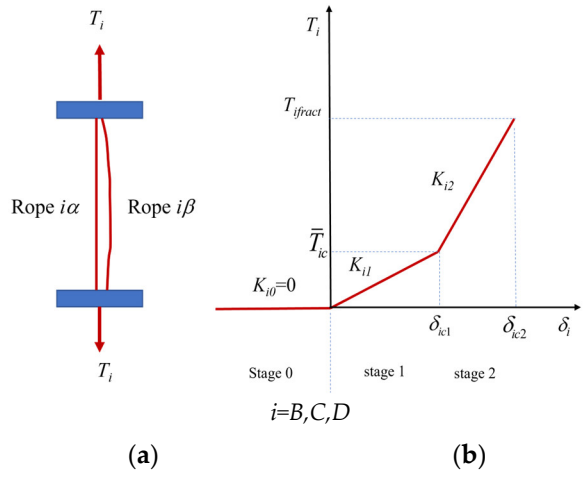

Figure 2. Effective spring constant of the main rope integrated by two parallel smaller ropes with different lengths. (**a**) Two integrated ropes in parallel; (**b**) effective spring constant K_i elongation relation δ_i.

The total tension of rope A is

$$T_A(t) = \begin{cases} 0, & \delta_A < 0 \\ K_A\delta_A, & 0 \le \delta_A \end{cases}, \tag{6}$$

where the total elongation of rope A is $\delta_A = \delta_{As} + \delta_{Ad}$, the static elongation is $\delta_{As} = T_{As}/K_A$, and the dynamic elongation is $\delta_{Ad} = \frac{x_{1s}}{L_A}x_{1d} + \frac{y_{1s}}{L_A}y_{1d}$.

The total tension of rope B is

$$T_B(t) = \begin{cases} 0, & \delta_B < 0 \\ \overline{K}_{B\alpha}\delta_{Bd}, & 0 \le \delta_B < \delta_{Cc1}, \\ \overline{K}_{B\alpha}\left(\delta_{Bc1} + \delta_{B\beta}\right) + \overline{K}_{B\beta}\delta_{B\beta}, & \delta_B \ge \delta_{Bc1} \end{cases} \tag{7}$$

where the total elongation of rope B is $\delta_B = \delta_{Bs} + \delta_{Bd}$, the static elongation is $\delta_{Bs} = T_{Bs}/\overline{K}_{Ba}$, and the dynamic elongation is $\delta_{\mathrm{Bd}} = \frac{x_{1s}-x_{2s}}{L_B}(x_{1d} - x_{2d}) + \frac{y_{1s}-y_{2s}}{L_B}(y_{1d} - y_{2d})$.

The total tension of rope C is

$$T_C(t) = \begin{cases} 0, & \delta_C < 0 \\ \overline{K}_{C\alpha}\delta_{Cd}, & 0 \le \delta_C < \delta_{Cc1}, \\ \overline{K}_{C\alpha}\left(\delta_{Cc1} + \delta_{C\beta}\right) + \overline{K}_{C\beta}\delta_{C\beta}, & \delta_C \ge \delta_{Cc1} \end{cases} \tag{8}$$

where the total elongation of rope C is $\delta_C = \delta_{Cs} + \delta_{Cd}$, the static elongation is $\delta_{Cs} = T_{Cs}/\overline{K}_{Ca}$, and the dynamic elongation is $\delta_{Cd} = x_{3d}(t) - x_{1d}(t)$.

The total tension of rope D is

$$T_D(t) = \begin{cases} 0, & \delta_D < 0 \\ \overline{K}_{D\alpha}\delta_D, & 0 \le \delta_D < \delta_{Dc1}, \\ \overline{K}_{D\alpha}\left(\delta_{Dc1} + \delta_{D\beta}\right) + \overline{K}_{D\beta}\delta_{D\beta}, & \delta_D \ge \delta_{Dc1} \end{cases} \tag{9}$$

where the total elongation of rope D is $\delta_D = \delta_{Ds} + \delta_{Dd}$, the static elongation is $\delta_{Ds} = T_{Ds}/\overline{K}_{Da}$, and the dynamic elongation is $\delta_{Dd} = x_{4d}(t) - x_{2d}(t)$.

2.2.2. Strain Energy, Effective Spring Constant, and Fracture Strength

The fracture strength of the rope is designated as $T_{fract,i}$. The fracture strength of rope $i\alpha$ is $\overline{T}_{fract,i\alpha}$. The tension of rope $i\beta$ is $\overline{T}_{fract,i\beta}$ when rope $i\alpha$ is at the broken point. The relations among tensions, effective spring constants, and the elongations can be expressed as

$$T_{frac,i} = \overline{T}_{frac,i\alpha} + \overline{T}_{frac,i\beta} = \gamma_{i\alpha}T_{frac,i} + (1 - \gamma_{i\alpha})T_{frac,i} \tag{10}$$

$$\overline{T}_{frac,i\alpha} = \overline{K}_{i\alpha}\delta_{ic2}, \overline{T}_{frac,i\beta} = \overline{K}_{i\beta}(\delta_{ic2} - \delta_{ic1}) \tag{11}$$

where the fracture strength ratio is $\gamma_{i\alpha} = \overline{T}_{frac,i\alpha}/T_{frac,i}$. δ_{ic2} is the fracture elongation of rope $i\alpha$. δ_{ic1} is the critical elongation of rope $i\alpha$ at which the tension stage 1 transforms into stage 2.

It is assumed that the fracture strain of rope $i\alpha$ and the strain of rope $i\beta$ when rope $i\alpha$ is broken are, respectively,

$$\varepsilon_{i\alpha} = \overline{T}_{frac,i\alpha}/E_{i\alpha}A_{i\alpha}, \text{ and } \varepsilon_{i\beta} = \overline{T}_{frac,i\beta}/E_{i\beta}A_{i\beta} \tag{12}$$

The lengths of ropes $i\alpha$ and $i\beta$ are

$$L_{i\alpha} = L_i,\ L_{i\beta} = L_{i\alpha} + \delta_{ic1} \tag{13}$$

The effective spring constant of ropes $i\alpha$ and $i\beta$ are

$$\overline{K}_j = E_jA_j/L_j,\ j = i\alpha,\ i\beta \tag{14}$$

Based on Equations (11)–(13), one obtains

$$\delta_{ic2} = \varepsilon_{i\alpha} L_i, \tag{15}$$

$$(\delta_{ic2} - \delta_{ic1}) = \varepsilon_{i\beta}(L_i + \delta_{ic1}) \tag{16}$$

Substituting Equation (15) into Equation (16), one obtains

$$\delta_{ic1} = \frac{\varepsilon_{i\alpha} - \varepsilon_{i\beta}}{1 + \varepsilon_{i\beta}} L_i \tag{17}$$

Based on $\left\{\delta_{ic1},\ \delta_{ic2},\ \gamma_{i\alpha},\ \overline{T}_{frac,i\alpha},\ \overline{T}_{frac,i\beta}\right\}$, the fracture energy is determined to be

$$e_{frac,i} = \frac{1}{2}\overline{T}_{frac,i\alpha}\delta_{ic2} + \frac{1}{2}\overline{T}_{frac,i\beta}(\delta_{ic2} - \delta_{ic1}) = \frac{1}{2}\overline{T}_{frac,i} L_i \left[\varepsilon_{i\beta} + (\varepsilon_{i\beta} + \gamma_{i\alpha})\frac{\varepsilon_{i\alpha} - \varepsilon_{i\beta}}{1 + \varepsilon_{i\beta}}\right] \tag{18}$$

In general, the higher the fracture energy of a rope is, the safer the rope subjected to a given tension will be.

2.3. Examples of Integrated Ropes

Example 1: The properties of a commercial HSPE rope are as follows: Young's modulus E_{PE} = 100 GPa, weight per unit length w_{PE} = 16.22 kg/m, diameter D_{PE} = 154 mm, cross-sectional area A_{PE} = 0.0186 m^2, length L_{PE} = 300 m, fracture strength $T_{\mathrm{frac,PE}}$ = 759 tons. The fracture strain $\varepsilon_{\mathrm{fract,PE}} = T_{\mathrm{frac,PE}}/E_{\mathrm{PE}}A_{\mathrm{PE}} = 0.004$. The effective spring constant $K_{PE} = E_{PE}A_{PE}/L_{PE} = 632(\mathrm{tons/m})$.

Assume rope i is made of two parallel smaller ropes, $i\alpha$ and $i\beta$. Based on the properties of the commercial HSPE rope, it can be assumed that the fracture strain of rope $i\alpha$ is $\varepsilon_{\mathrm{frac},i\alpha} = \overline{T}_{\mathrm{frac},i\alpha}/E_{i\alpha}A_{i\alpha} = 0.004$. The strain of rope $i\beta$ when rope $i\alpha$ is broken but rope $i\beta$ is safe is $\varepsilon_{\mathrm{frac},i\beta} = \overline{T}_{\mathrm{frac},i\beta}/E_{i\beta}A_{i\beta} = 0.002$. The fracture strength and length of the integrated rope are considered to be $T_{\mathrm{frac},i}$ =750 tons and L_i = 300 m, respectively.

Figure 3 demonstrates the effect of the ratio $\gamma_{i\alpha}$ of the fracture strength of the rope $i\alpha$ to that of the integrated rope on the effective spring constants of the integrated rope $\{K_{i1}, K_{i2}\}$, the critical elongations $\{\delta_{ic1}, \delta_{ic2}\}$, the transformed tension T_{trans}, and the fracture energy of the integrated rope $e_{\mathrm{frac,i}}$. It was found that if the elongation $\delta_i < \delta_{ic1} = 0.597$ m, only rope $i\alpha$ will be working, and the effective spring constant K_{i1} increases with fracture strength ratio $\gamma_{i\alpha}$. If the elongation $\delta_{ic1} < \delta_i < \delta_{ic2} = 1.196$ m, ropes $i\alpha$ and $i\beta$ will be simultaneously subjected to loads. If the elongation $\delta_i \geq \delta_{ic2}$, the rope $i\alpha$ will be broken but not rope $i\beta$. The higher the fracture strength ratio $\gamma_{i\alpha}$, the larger the fracture energy $e_{\mathrm{frac,i}}$. If the fracture strength ratio $\gamma_{i\alpha} = 0.8$, the fracture energy $e_{\mathrm{frac,i}} = 403.8$ (tons-m). The higher the fracture strength ratio $\gamma_{i\alpha}$, the larger the effective spring constant of rope $i\alpha$. In other words, the buffering effect decreases with decreasing fracture strength ratio $\gamma_{i\alpha}$. If the elongation $\delta_i < \delta_{ic1} = 0.597$ m, only rope $i\alpha$ will be working, and the effective spring constant K_{i1} will be significantly lower than that of the commercial HSPE dyneema, K_{PE}= 632 (tons/m). Therefore, a significant application of the buffering effect of impact was achieved by the integration of parallel ropes.

Example 2: If the length of the commercial HSPE dyneema with $T_{\mathrm{frac,PE}}$ = 759 tons, L_{PE} = 100 m, its effective spring constant K_{PE} =1896 (tons/m).

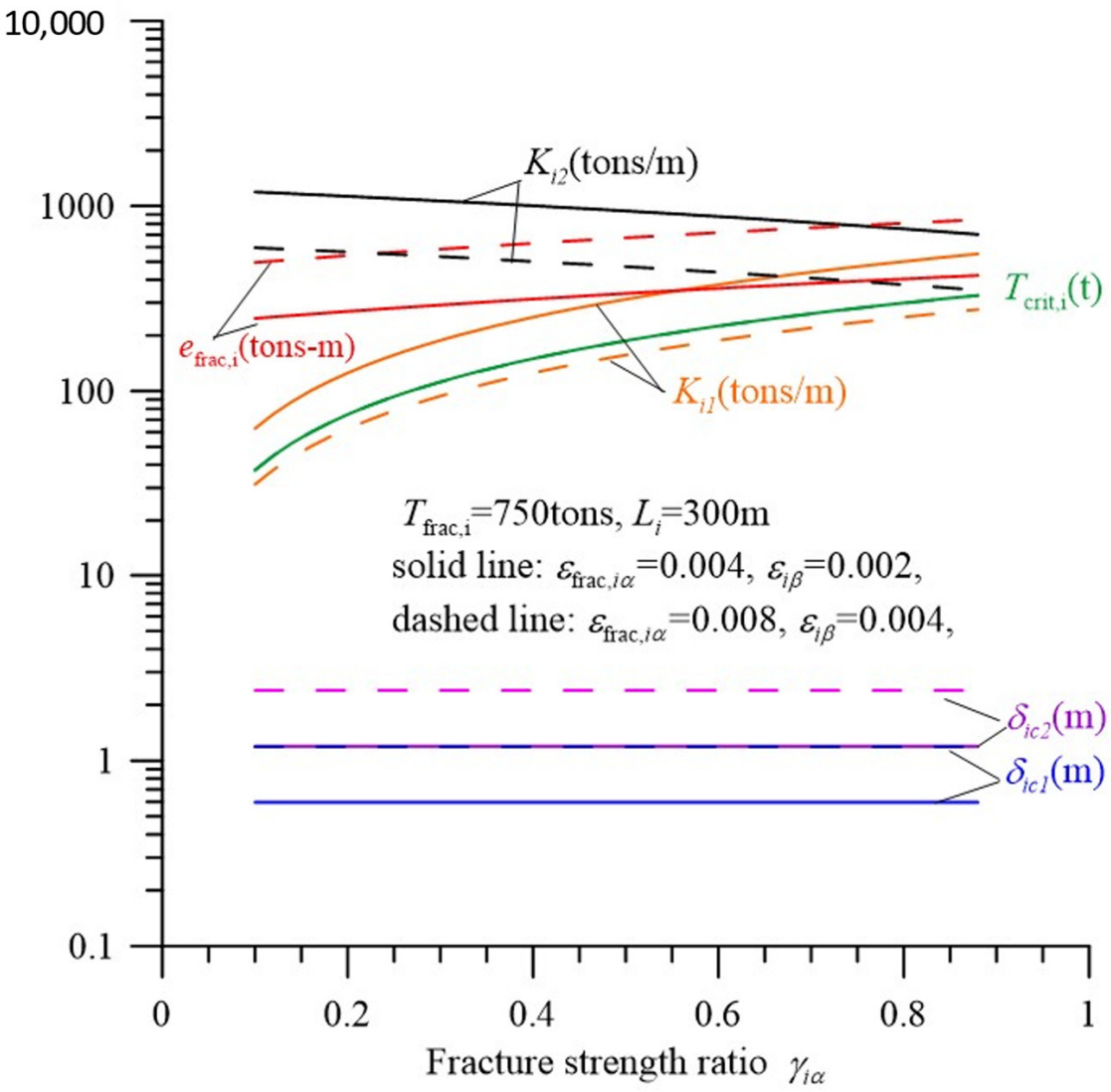

Figure 3. The effect of fracture strength ratio on the properties of integrated rope with $T_{frac,i}$ = 750 tons and L_i = 300 m.

In Figure 4, it is considered that when rope $i\alpha$ is broken, the fracture strain of rope $i\alpha$, $\varepsilon_{frac,i\alpha}$ = 0.004, and the strain of rope $i\beta$, $\varepsilon_{frac,i\beta}$= 0.002. The fracture strength and length of the integrated rope $T_{frac,i}$ = 550 tons and L_i = 100 m, respectively. Figure 4 shows the critical elongations δ_{ic1} =0.199 m, δ_{ic2} =0.399 m, which are less than those in Figure 3. If the fracture strength ratio $\gamma_{i\alpha}$ = 0.8, the fracture energy $e_{frac,i}$ = 98.7 (tons-m), which is smaller than that in Figure 3 due to the fracture strength and length of the rope. If the elongation $\delta_i < \delta_{ic1}$ = 0.199 m, only rope a will be working, and the effective spring constant K_1 will be significantly smaller than that of the commercial HSPE dyneema, K_{PE} = 1896 (tons/m). Therefore, the significant application of a buffering effect of impact was achieved through the integration of parallel ropes. When considering the double-rope parallel mode, the stiffness coefficients K_{ij} depend on the dynamic tension of ropes, i.e., the stiffness coefficients are time-varying, as shown in Equation (2). In this study, the solution method derived for solving the mooring system with time-varying coefficients will be presented later.

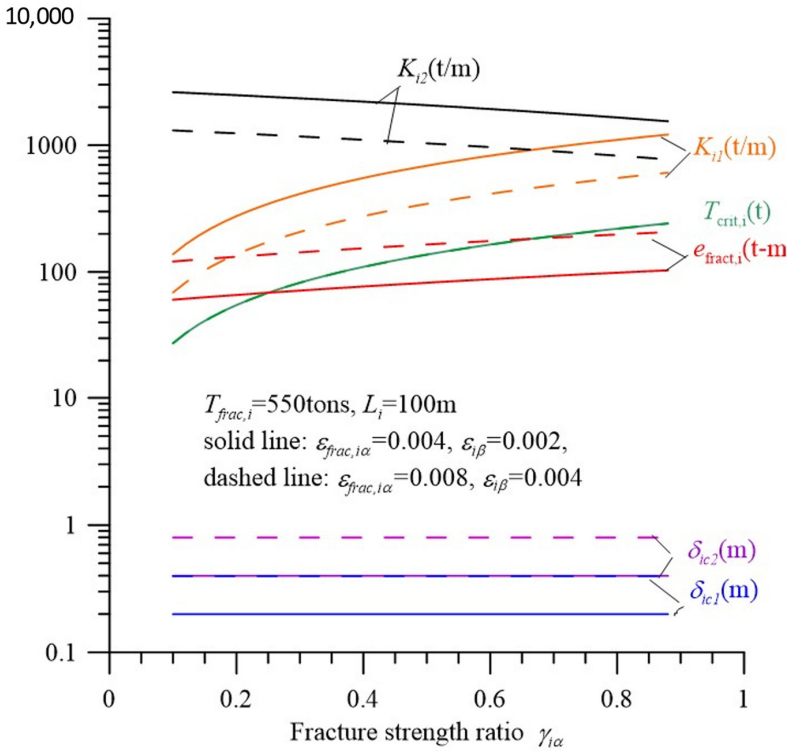

Figure 4. Effect of fracture strength ratio on the properties of the integrated rope with $T_{\text{frac,i}}$ = 550 tons and L_i = 100 m.

3. Solution Method

3.1. Transient Response

The governing Equation (1) in matrix format is composed of 18 second-order ordinary differential equations, as presented by Lin et al. [8]. Because there are two independent fundamental solutions for a second-order ordinary differential equation, 36 independent fundamental solutions exist for Equation (1). The general solution of Equation (1) can be expressed as the linear combination of 36 independent fundamental solutions:

$$\mathbf{Z}_d(t) = \sum_{i=1}^{36} q_i \begin{bmatrix} V_{i,1}(t) \\ V_{i,2}(t) \\ \vdots \\ V_{i,18}(t) \end{bmatrix} \tag{19}$$

where the independent fundamental solutions, $\begin{bmatrix} V_{i,1}(t) & V_{i,2}(t) & \cdots & V_{i,18}(t) \end{bmatrix}^T, i = 1, 2, \ldots, 36$, satisfy the governing Equation (1) and the following normalized condition:

$$\begin{bmatrix} \begin{bmatrix} V_{1,1} \\ V_{1,2} \\ \vdots \\ V_{1,18} \end{bmatrix} & \begin{bmatrix} V_{2,1} \\ V_{2,2} \\ \vdots \\ V_{2,18} \end{bmatrix} & \cdots & \begin{bmatrix} V_{35,1} \\ V_{35,2} \\ \vdots \\ V_{35,18} \end{bmatrix} & \begin{bmatrix} V_{36,1} \\ V_{36,2} \\ \vdots \\ V_{36,18} \end{bmatrix} \\ \begin{bmatrix} \dot{V}_{1,1} \\ \dot{V}_{1,2} \\ \vdots \\ \dot{V}_{1,18} \end{bmatrix} & \begin{bmatrix} \dot{V}_{2,1} \\ \dot{V}_{2,2} \\ \vdots \\ \dot{V}_{2,18} \end{bmatrix} & \cdots & \begin{bmatrix} \dot{V}_{35,1} \\ \dot{V}_{35,2} \\ \vdots \\ \dot{V}_{35,18} \end{bmatrix} & \begin{bmatrix} \dot{V}_{36,1} \\ \dot{V}_{36,2} \\ \vdots \\ \dot{V}_{36,18} \end{bmatrix} \end{bmatrix}_{t=0} = \begin{bmatrix} 1 & 0 & \cdots & 0 & 0 \\ 0 & 1 & \cdots & 0 & 0 \\ \vdots & \vdots & \ddots & \vdots & \vdots \\ 0 & 0 & \cdots & 1 & 0 \\ 0 & 0 & \cdots & 0 & 1 \end{bmatrix} \tag{20}$$

Substituting the solution (19) into the initial conditions (3–4), one obtains

$$\mathbf{Z}_d(0) = \sum_{i=1}^{2n} q_i \begin{bmatrix} V_{i,1}(0) \\ V_{i,2}(0) \\ \vdots \\ V_{i,18}(0) \end{bmatrix}, \quad \frac{d\mathbf{Z}_d(0)}{dt} = \sum_{i=1}^{36} q_i \begin{bmatrix} \dot{V}_{i,1}(0) \\ \dot{V}_{i,2}(0) \\ \vdots \\ \dot{V}_{i,18}(0) \end{bmatrix} \tag{21}$$

Based on Equation (21) and the normalized condition, one obtains the coefficients q_i, $i = 1, 2, \ldots, 36$.

$$\begin{bmatrix} q_1 \\ q_2 \\ \vdots \\ q_{35} \\ q_{36} \end{bmatrix} = \begin{bmatrix} \mathbf{Z}_d(0) \\ \frac{d\mathbf{Z}_d(0)}{dt} \end{bmatrix} \tag{22}$$

3.2. Derivation of a Fundamental Solution

If ropes B, C, and/or D are integrated with two more ropes in parallel, their stiffness spring constant and the elements of the stiffness matrix will vary with time. Therefore, it is difficult to directly derive the fundamental solutions of Equation (1). A semi-analytical method is proposed as follows:

The time interval $(0, t_f)$ is divided into m small subintervals, $(t_0, t_1), (t_1, t_2), \cdots, \left(t_{m-1}, t_m = t_f\right)$. If the number of subinterval m is large enough, the elements of the stiffness matrix are close to constant in each subinterval. Furthermore, one can derive the independent and normalized fundamental solution by using the modified Frobenius method.

In the small subinterval (t_{e-1}, t_e), the 36 independent fundamental solutions of Equation (1) are expressed in the form of

$$\begin{bmatrix} \overline{V}_{j,1} \\ \overline{V}_{j,2} \\ \vdots \\ \overline{V}_{j,18} \end{bmatrix} = \sum_{i=0}^{\infty} \begin{bmatrix} \overline{\alpha}_{j,1,i} \\ \overline{\alpha}_{j,2,i} \\ \vdots \\ \overline{\alpha}_{j,18,i} \end{bmatrix} (t - t_{e-1})^i, \qquad j = 1, 2 \ldots, 36 \tag{23}$$

For $\overline{V}_{1,1}$: $\overline{\alpha}_{1,1,0} = 1, \overline{\alpha}_{1,1,1} = 0$
For $\overline{V}_{2,1}$: $\overline{\alpha}_{2,1,0} = \overline{\alpha}_{2,1,1} = 0$,
For $\overline{V}_{k,1}$: $\overline{\alpha}_{k,1,0} = \overline{\alpha}_{k,1,1} = 0$, $k = 2, 3, \ldots, n$
For $\overline{V}_{2,2}$: $\overline{\alpha}_{2,2,0} = 1, \overline{\alpha}_{2,2,1} = 0$
For $\overline{V}_{k,2}$: $\overline{\alpha}_{k,2,0} = \overline{\alpha}_{k,2,1} = 0$, $k = 1, 3, 4, \ldots, n$
For $\overline{V}_{k,k}$: $\overline{\alpha}_{k,k,0} = 1, \overline{\alpha}_{k,k,1} = 0$, $k = 1, 2, \ldots, n$
For $\overline{V}_{j,k}$: $\overline{\alpha}_{j,k,0} = \overline{\alpha}_{j,k,1} = 0$, $j = 1, 2, \ldots, k-1, k+1, k+2, \ldots, n$
For $\overline{V}_{k,n+k}$: $\overline{\alpha}_{k,n+k,1} = 1, \overline{\alpha}_{k,n+k,0} = 0, k = 1, 2, \ldots, n$
For $\overline{V}_{j,n+k}$: $\overline{\alpha}_{j,n+k,0} = \overline{\alpha}_{j,n+k,1} = 0$, $j = 1, 2, \ldots, k-1, k+1, k+2, \ldots, n$ (24)

Based on Equations (23) and (24), the local fundamental solutions satisfy the following normalized condition:

$$\begin{bmatrix} \begin{bmatrix} \overline{V}_{1,1} \\ \overline{V}_{2,1} \\ \vdots \\ \overline{V}_{n,1} \end{bmatrix} & \begin{bmatrix} \overline{V}_{1,2} \\ \overline{V}_{2,2} \\ \vdots \\ \overline{V}_{n,2} \end{bmatrix} & \cdots & \begin{bmatrix} \overline{V}_{1,2n-1} \\ \overline{V}_{2,2n-1} \\ \vdots \\ \overline{V}_{n,2n-1} \end{bmatrix} & \begin{bmatrix} \overline{V}_{1,2n} \\ \overline{V}_{2,2n} \\ \vdots \\ \overline{V}_{n,2n} \end{bmatrix} \\ \begin{bmatrix} \dot{\overline{V}}_{1,1} \\ \dot{\overline{V}}_{2,1} \\ \vdots \\ \dot{\overline{V}}_{n,1} \end{bmatrix} & \begin{bmatrix} \dot{\overline{V}}_{1,2} \\ \dot{\overline{V}}_{2,2} \\ \vdots \\ \dot{\overline{V}}_{n,2} \end{bmatrix} & \cdots & \begin{bmatrix} \dot{\overline{V}}_{1,2n-1} \\ \dot{\overline{V}}_{2,2n-1} \\ \vdots \\ \dot{\overline{V}}_{n,2n-1} \end{bmatrix} & \begin{bmatrix} \dot{\overline{V}}_{1,2n} \\ \dot{\overline{V}}_{2,2n} \\ \vdots \\ \dot{\overline{V}}_{n,2n} \end{bmatrix} \end{bmatrix}_{t=t_{e-1}} = \begin{bmatrix} 1 & 0 & \cdots & 0 & 0 \\ 0 & 1 & \cdots & 0 & 0 \\ \vdots & \vdots & \ddots & \vdots & \vdots \\ 0 & 0 & \cdots & 1 & 0 \\ 0 & 0 & \cdots & 0 & 1 \end{bmatrix} \tag{25}$$

Substituting (23) into (1), and according to Equation (24), the recurrence Formula (17) is obtained.

$$\overline{\alpha}_{j,g,i+2} = \frac{-1}{(i+2)(i+1)M_{gg}} \left[\sum_{s=1}^{18} (i+1)\overline{\alpha}_{j,s,i+1} C_{gs} + \sum_{s=1}^{18} \overline{\alpha}_{j,s,i} K_{gs} \right], \quad i = 0,\ 1,\ \ldots,\ j = 1,\ 2,\ \ldots,\ 36, g = 1,\ 2,\ \ldots,\ 18 \tag{26}$$

The coefficients of the fundamental solutions (23) can be determined via this Formula (26).

In the subdomain (t_{e-1}, t_e), each global fundamental solution can be linearly composed of the 36 local independent fundamental solutions (23).

$$\begin{bmatrix} V_{j,1} \\ V_{j,2} \\ \vdots \\ V_{j,18} \end{bmatrix}_{t\in(t_{e-1},t_e)} = \sum_{a=1}^{36} \chi_{ja,e} \begin{bmatrix} \overline{V}_{a,1} \\ \overline{V}_{a,2} \\ \vdots \\ \overline{V}_{a,18} \end{bmatrix}_{t\in(t_{e-1},t_e)}, j = 1,\ 2,\ \ldots,\ 36 \tag{27}$$

The continuity conditions are as follows:

$$\begin{bmatrix} V_{j,1} \\ V_{j,2} \\ \vdots \\ V_{j,18} \end{bmatrix}_{t=t_{e-1}} = \sum_{a=1}^{36} \chi_{ja} \begin{bmatrix} \overline{V}_{a,1} \\ \overline{V}_{a,2} \\ \vdots \\ \overline{V}_{a,18} \end{bmatrix}_{t=t_{e-1}}, \begin{bmatrix} \dot{V}_{j,1} \\ \dot{V}_{j,2} \\ \vdots \\ \dot{V}_{j,18} \end{bmatrix}_{t=t_{e-1}} = \sum_{a=1}^{36} \chi_{ja} \begin{bmatrix} \dot{\overline{V}}_{a,1} \\ \dot{\overline{V}}_{a,2} \\ \vdots \\ \dot{\overline{V}}_{a,18} \end{bmatrix}_{t=t_{e-1}}, \ j = 1,\ 2,\ \ldots,\ 36 \tag{28}$$

Based on the continuity conditions (28), the coefficients of Equation (27) can be determined:

$$\begin{bmatrix} \chi_{1,1,e} & \chi_{2,1,e} & \cdots & \chi_{35,1,e} & \chi_{36,1,e} \\ \chi_{1,2,e} & \chi_{2,2,e} & \cdots & \chi_{35,2,e} & \chi_{36,2,e} \\ \vdots & \vdots & \vdots & \vdots & \vdots \\ \chi_{1,35,e} & \chi_{2,2n-1,e} & \cdots & \chi_{35,351,e} & \chi_{36,35,e} \\ \chi_{1,36,e} & \chi_{2,2n,e} & \cdots & \chi_{35,36,e} & \chi_{36,36,e} \end{bmatrix}_{t\in(t_{e-1},t_e)} = \begin{bmatrix} \begin{bmatrix} V_{1,1} \\ V_{1,2} \\ \vdots \\ V_{1,18} \end{bmatrix} & \begin{bmatrix} V_{2,1} \\ V_{2,2} \\ \vdots \\ V_{2,18} \end{bmatrix} & \cdots & \begin{bmatrix} V_{35,1} \\ V_{35,2,} \\ \vdots \\ V_{35,18} \end{bmatrix} & \begin{bmatrix} V_{36,1} \\ V_{36,2} \\ \vdots \\ V_{36,18} \end{bmatrix} \\ \begin{bmatrix} \dot{V}_{1,1} \\ \dot{V}_{1,2} \\ \vdots \\ \dot{V}_{1,18} \end{bmatrix} & \begin{bmatrix} \dot{V}_{2,1} \\ \dot{V}_{2,2} \\ \vdots \\ \dot{V}_{2,18} \end{bmatrix} & \cdots & \begin{bmatrix} \dot{V}_{35,1} \\ \dot{V}_{35,2} \\ \vdots \\ \dot{V}_{35,18} \end{bmatrix} & \begin{bmatrix} \dot{V}_{36,1} \\ \dot{V}_{36,2} \\ \vdots \\ \dot{V}_{36,18} \end{bmatrix} \end{bmatrix}_{t=t_{e-1}} \tag{29}$$

According to Equations (23), (27), and (29), all of the global fundamental solutions are determined. Furthermore, substituting these back into Equation (19) and the initial conditions (3–4) and (22), the transient translational and angular displacements of platform 1, inverter 2, and pontoons 3 and 4 are determined.

4. Numerical Results and Discussion

4.1. Effects of Initial Displacements, Effective Spring Constant, and Double-Rope Parallel Mode

Firstly, in Figure 5, the transient response of the mooring system with the initial conditions (30) is presented. The initial translational and rotational displacements are as follows:

$$\mathbf{Z}_d|_{t=0} = \begin{bmatrix} x_{1d0} & y_{1d0} & z_{1d0} & x_{2d0} & y_{2d0} & z_{2d0} & x_{3d0} & y_{3d0} & z_{3d0} & x_{4d0} & y_{4d0} & z_{4d0} & \varphi_{Tx0} & \varphi_{Ty0} & \varphi_{Tz0} & \varphi_{Px0} & \varphi_{Py0} & \varphi_{Pz0} \end{bmatrix}^T = \begin{bmatrix} 7.192 & -0.013 & 3.6 & 18 & 0 & 3.6 & 7.198 & 3.6 & 0 & 18 & 3.6 & 0 & 0 & 0 & 0 & 0 & 0 & 0 \end{bmatrix}^T (\text{m; rad}) \quad (30)$$

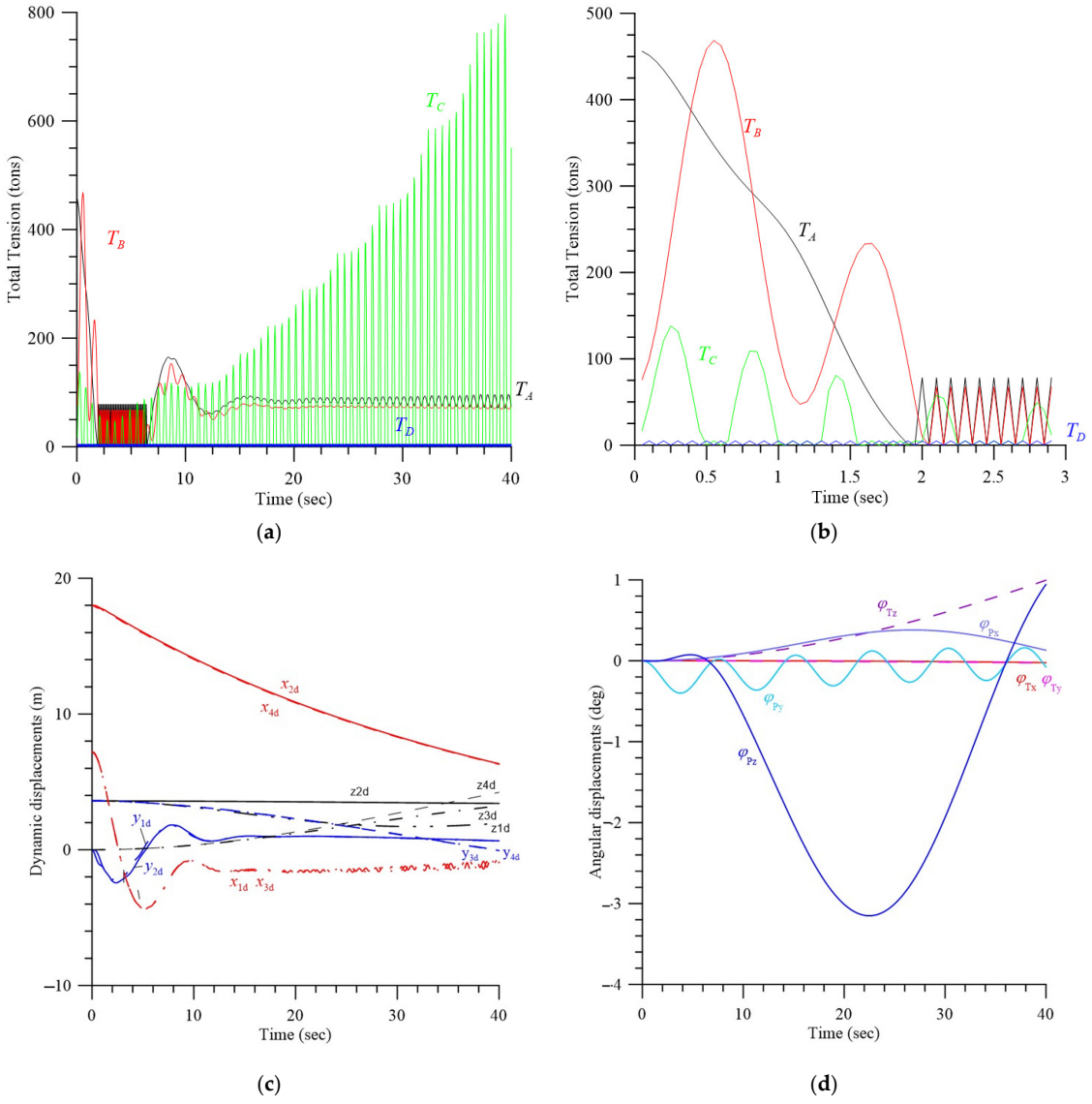

Figure 5. Transient response of mooring system with $L_C = L_D = 100$ m, $K_{Cd} = K_{Dd} = 1889$ (tons/m). (**a**) Total tension of ropes (I). (**b**) Total tension of ropes (II). (**c**) Displacements of pontoons, turbine, and platform. (**d**) Angular displacements of turbine and platform.

These are mainly the initial displacements in the x-direction of platform 1, inverter 2, and pontoons 3 and 4, deviating from the neutral position. The initial (angular) velocities are zero as follows:

$$\dot{\mathbf{Z}}_d\Big|_{t=0} = \begin{bmatrix} \dot{x}_{1d0} & \dot{y}_{1d0} & \dot{z}_{1d0} & \dot{x}_{2d0} & \dot{y}_{2d0} & \dot{z}_{2d0} & \dot{x}_{3d0} & \dot{y}_{3d0} & \dot{z}_{3d0} & \dot{x}_{4d0} & \dot{y}_{4d0} & \dot{z}_{4d0} & \dot{\varphi}_{Tx0} & \dot{\varphi}_{Ty0} & \dot{\varphi}_{Tz0} & \dot{\varphi}_{Px0} & \dot{\varphi}_{Py0} & \dot{\varphi}_{Pz0} \end{bmatrix}^T = \begin{bmatrix} 0 & \cdots & 0 \end{bmatrix}^T \quad (31)$$

On the basis of these initial conditions, the dynamic behavior of the system can be observed to revert back to the neutral position in order to investigate the stability of the mooring system.

The parameters of the system are listed in Table 1. The ropes *A*, *B*, *C*, and *D* are made of the same HSPE, the fracture strength of which is T_{frac} = 759 tons. The hydrodynamic damping coefficients of platform 1, inverter 2, and pontoons 3 and 4 are listed in Appendix B. The hydrodynamic damping coefficients $C_{3,3} = 5756$(N-s/m), $C_{4,4} = 1.465 \times 10^6$(N-s/m), $C_{7,7} = C_{10,10} = 300$(N-s/m).

Table 1. The parameters of the system.

Parameter		Dimension	Parameter	Dimension
depth of seabed H_{bed}		1000 m	length of rope *C*, L_C	100 m
length of rope *D*, L_D		100 m	horizontal distance between the inverter and platform L_E	300 m
inclined angle of rope *A*, θ_A		30^0	mass moment of inertia of the convertor about the *x*, , -axis, $I_{Tx}/I_{Ty}/I_{Tz}$	8.940×10^{10}/ 2.712×10^{10}/ 8.940×10^{10}(kg-m^2)
cross-sectional area of surfaced cylinder of pontoon 3, A_{BX}		4 m^2	mass moment of inertia of the platform about the *x*, *y*, z-axis, $I_{Px}/I_{Py}/I_{Pz}$	$3.0 \times 10^8/5.0 \times 10^6$/ 3.0×10^8(kg-m^2)
cross-sectional area of surfaced cylinder of pontoon 4, A_{BT}		4 m^2	distance from the gravity of invertor to rope B, D, R_{TB}/R_{TD}	16.5/12.82 m
HSPE rope	Young's modulus E_{PE}	100 GPa,	current velocity *V*	1.6 m/s
	weight per unit length w_{PE}	16.22 kg/m	mass of the platform M_1	300 tons
	diameter D_{PE}	154 mm	mass of the invertor M_2	538 tons
	cross-sectional area A_{PE}	0.0186 m^2	mass of the pontoon 3, M_3	250 tons
	fracture strength T_{frac}	759 tons	mass of the pontoon 4, M_4	250 tons
distance from the gravity of platform to ropes *A*, *B*, *C*, $R_{PA}/R_{PB}/R_{PC}$		5/5.8/2.5 m	static tension of ropes *A*, *B*, *C*, *D*, $T_{As}/T_{Bs}/T_{Cs}/T_{Ds}$	78.07/67.53/5/5 tons
static drag of the invertor F_{DT}		67.53 tons	net buoyance of invertor and platform F_{BNT}/F_{BNB}	533/320.77 tons

The maximum power coefficient of cost performance (*CP*) of the proposed turbine is 0.43 at a tip-speed ratio (*TSR*) = 3.5. When the current velocity *V* = 1.6 m/s, the total output power of the two turbines is close to 400 kW [8]. Obviously, the current profile changes with respect to time and depth. Due to the complexity of the presented theorem, and for the sake of clarity of the presented theory, a uniform current velocity was considered. Ropes *A*, *B*, *C*, and *D* are made of a single HSPE rope, the material and diameter of which are the same as those listed in Table 1. Based on the formula $K_d = EA./L$, the effective spring constant K_{Ad} =105.3 (tons/m), K_{Bd} =631.3 (tons/m), $K_{Cd} = K_{Dd}$ =1889 (tons/m). The effective spring constants of ropes *B*, *C*, and *D* are significantly higher than that of rope *A*, because the lengths of *B*, *C* and *D* are very short and the diameter and fracture strength

of ropes A, B, C, and D are the same. The transient responses are determined and shown in Figure 5a–d.

Figure 5a,b show that, initially, the transient tensions of ropes A and B, T_A and T_B, are very high. Furthermore, these tensions gradually converge to low values. However, the tension of rope C, T_C, increases gradually. This is because the effective spring constants of ropes B, C, and D are high, and their buffet effects are weak. It is demonstrated in Figure 5c that the displacements of the invertor and the pontoon 4 in the x-direction decay. The displacements of the platform and pontoon 3 in the x-direction oscillate and finally converge to about 1 m. It is demonstrated in Figure 5d that the yaw and roll angles of the invertor are close to zero. The pitch angle of the invertor is smaller than one degree at a time of 40 s. The pitch, yaw, and roll angles of the platform are higher than those of the invertor. Therefore, it is verified that, because the effective spring constants of ropes C and D are very high, their buffering feature is weak, and their instability will be easily obtained.

In order to overcome this disadvantage, ropes C and D are made of the same HSPE material as the other ropes, but with smaller diameters so that their effective spring constants will become significantly lower, while the fracture strength will decrease. In Figure 6, the effect of lowering the diameters of ropes C and D on the transient response of the mooring system is investigated. Ropes A and B are made of a single HSPE rope, described in Table 1. Their cross-sectional area was $A_A = A_B = 0.0186$ m^2. Their effective spring constants are the same as those in Figure 5. Ropes C and D are made of a single HSPE rope, the same as ropes A and B. However, their cross-sectional area was $A_C = A_D = 0.004$ m^2. Based on the linear elastic theory, the effective spring constant is reduced to $K_{Cd} = K_{Dd} = 412.2$ (tons/m). Their fracture strengths decrease to $T_{frac,j} = (A_j/A_i)T_{frac,i} = 162.54$ tons; $i = A,\ B, j = C,\ D$. Figure 6a shows that the tension of rope C converges to a lower value due to the lowering of the effective spring constants of ropes C and D. The maximum momentary tension of rope B is $T_{Bmax} = 464$ tons. The maximum momentary tension of rope C is $T_{Cmax} = 125.8$ tons, which is close to the fracture strength $T_{frac,C} = 162.54$ tons. Figure 6b shows that the transient displacements are stable and converge to the same value, as shown in Figure 5c. Therefore, it was verified that the lower the effective spring constants of ropes C and D are, the greater the stability of the mooring system. However, this design decreases the safety factor of the rope.

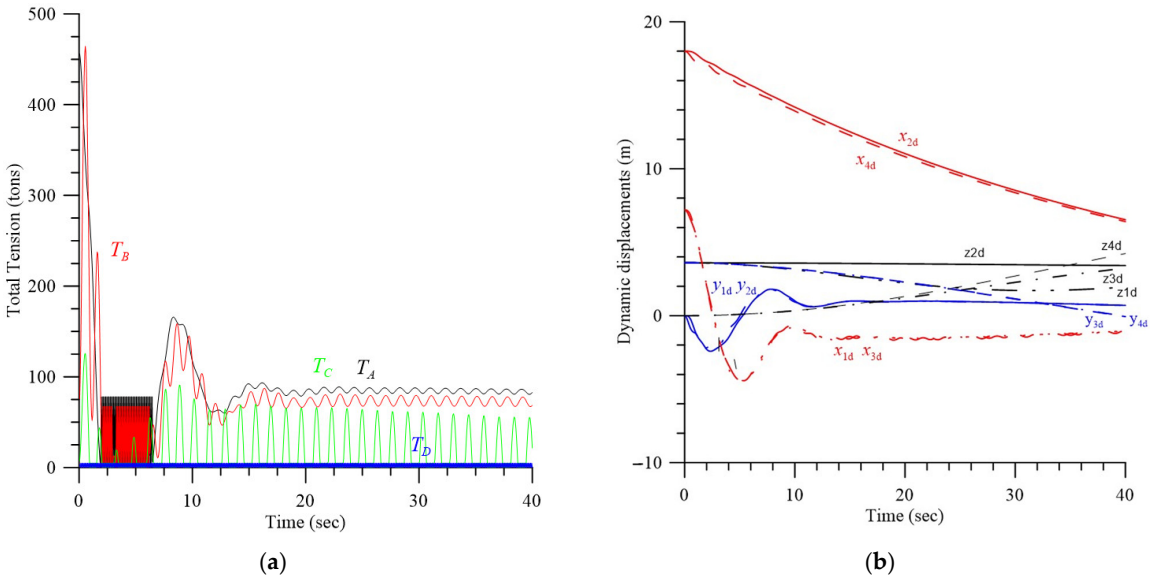

(**a**) (**b**)

Figure 6. Transient response of mooring system with $L_C = L_D = 100$ m, $K_{Cd} = K_{Dd} = 412.2$ (tons/m), $T_{frac,C} = T_{frac,D} = 162.54$ tons. (**a**) Total tension of ropes. (**b**) Displacements of pontoons, turbine, and platform.

In order to overcome the above disadvantage of low fracture strength, ropes *C* and *D* were designed in the double-rope parallel mode presented in Sections 2.2 and 2.3. This design results in the integrated rope possessing the features of a low effective spring constant and high fracture strength. The effective spring constants are K_{Ad} =105.3 (tons/m),K_{Bd} =631.3 (tons/m). The parameters of the integrated ropes *C*, *D* are $K_{j,stage1} = \overline{K}_{ja}$ = 689.7 (tons/m), T_{jc} =, 137 tons, $K_{j,stage2}$ =1394 (tons/m), *j* = *C*, *D*. The fracture strengths of ropes $T_{frac,A} = T_{frac,B}$ = 759 tons,$T_{frac,C} = T_{frac,D}$ =550 tons. It can be seen in Figure 7a that the maximum momentary tension of rope B is T_{Bmax} = 465 tons, which is close to that of Figure 6. It can be seen from Figure 7b that the displacements are stable and convergent. It was verified that the double-rope parallel mode is helpful for achieving system stability and high fracture strength.

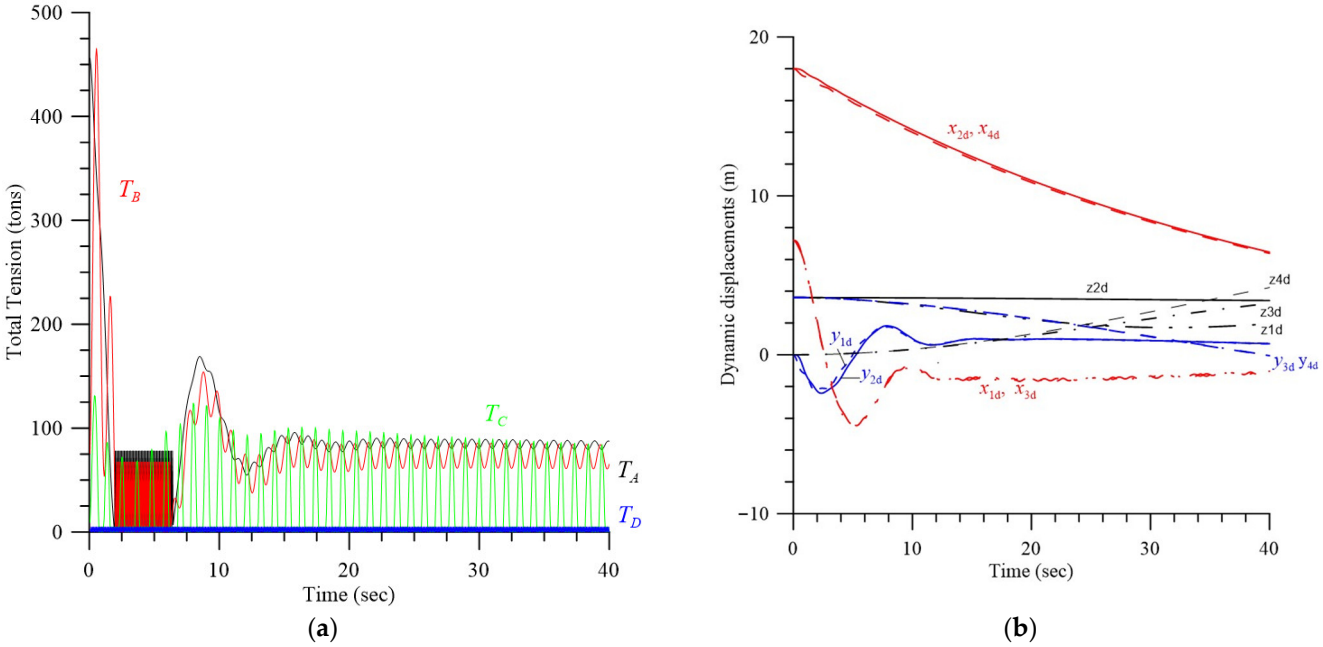

(**a**) (**b**)

Figure 7. Transient response of mooring system with $L_C = L_D$ = 100 m, $T_{frac,C} = T_{frac,D}$ = 550 tons. (**a**) Total tension of ropes. (**b**) Displacements of pontoons, turbine, and platform.

4.2. Effects of the Length of Rope and Hydrodynamic Heaving Damping

4.2.1. Transient Response and Improvement of Stability and Safety, L_C = 100 m, L_D = 110 m

The effect of variations in the length of ropes *C* and *D* on the transient response was investigated, and the results are shown in Figure 8. Except for L_C = 100 m, L_D = 110 m, the other parameters are the same as those used in Figure 6. The effective spring constants K_{Ad} =105.3 (tons/m), K_{Bd} =631.3 (tons/m), K_{Cd} =412.2 (tons/m),K_{Dd} = 403.4 (tons/m). The fracture strengths of ropes *A*, *B*, $T_{frac,A} = T_{frac,B}$ = 756 (tons). The fracture strengths of ropes *C*, *D*, $T_{frac,C} = T_{frac,D}$ = 162.54 tons. The hydrodynamic damping coefficients $C_{3,3}$ =5756 (N-s/m), $C_{4,4} = 1.465 \times 10^6$ (N-s/m), $C_{7,7} = C_{10,10}$ = 300 (N-s/m). It can be seen from Figure 8a that the tension of rope *B* is the greatest among ropes *A*, *B*, *C*, and *D*. The maximum momentary tension of rope *B* is T_{Bmax} = 617 tons, which is significantly larger than the T_{Bmax} = 464 tons shown in Figure 6, with $L_C = L_D$ = 100 m. It can be concluded that the effect of the lengths of ropes *C* and *D* on the maximum tension of rope *B* is significant. Figure 8b shows that the angular and translational displacements of the invertor are small. However, the swaying displacement z_{1d} of the platform increases significantly.

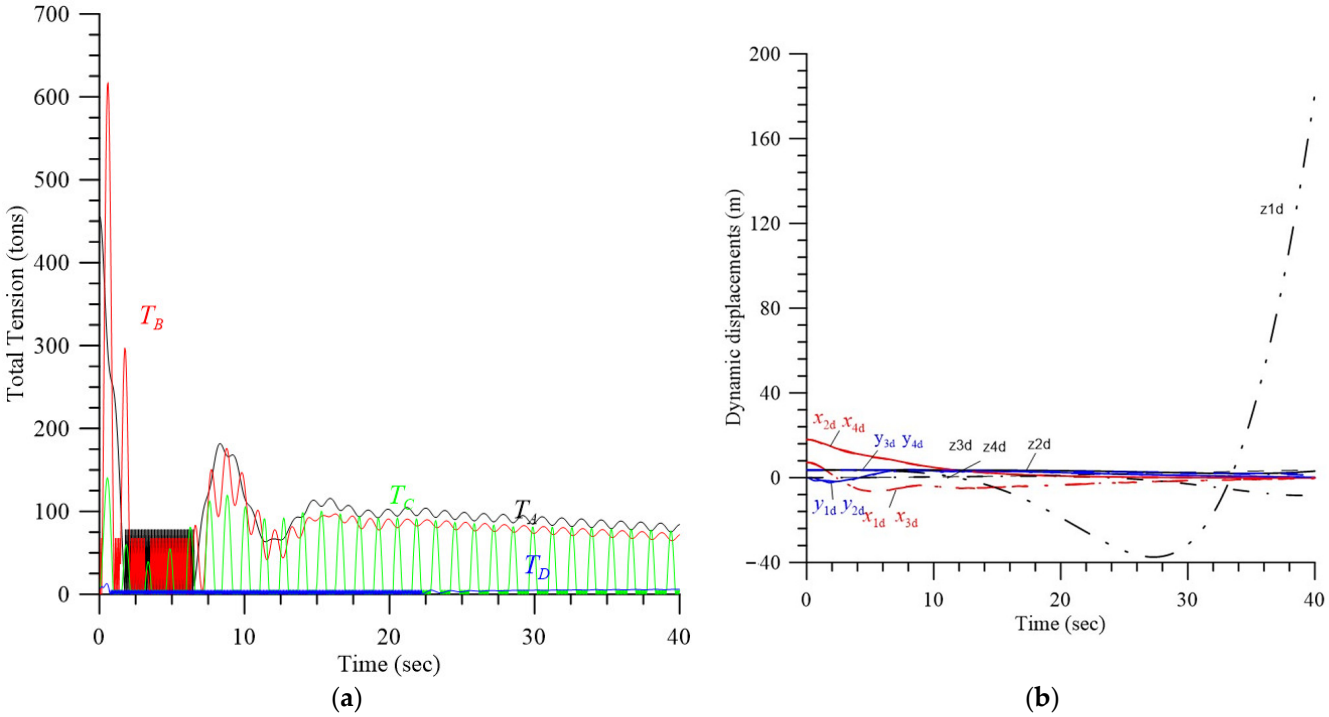

Figure 8. Transient response of mooring system with smaller diameters of ropes *C*, *D* [L_C = 100 m, L_D = 110 m, $T_{frac,C}$ = $T_{frac,D}$ = 162.54 tons]. (**a**) Total tension of ropes. (**b**) Displacements of pontoons, turbine, and platform.

It can be concluded by comparing Figures 6 and 8 that the effect of the lengths of ropes *C* and *D* on the transient response is significant.

In order to overcome the above disadvantages of the low fracture strength of ropes *C*, and *D*, the doubled-rope parallel mode derived in Sections 2.2 and 2.3 is proposed. This design results in a low effective spring constant and high fracture strength of the integrated rope. In Figure 9, the effective spring constant of rope *A* K_{Ad} =105.3 (tons/m). The parameters of the integrated ropes *B*, *C*, and *D* are $K_{B,stage1} = \overline{K}_{Ba}$ = 205 (tons/m), T_{Bc} =299 tons, $K_{B,stage2}$ =376.2 (tons/m), $K_{C,stage1} = \overline{K}_{Ca}$ =344.8 (tons/m), T_{Cc} =136 tons, $K_{C,stage2}$ = 1048 (tons/m), $K_{D,stage1} = \overline{K}_{Da}$ =131.5 (tons/m), T_{Dc} =137 tons, $K_{D,stage2}$ =940 (tons/m), and the fracture strengths of ropes *A*, *B*, $T_{frac,A}$ = $T_{frac,B}$ = 750 tons. The fracture strengths of ropes *C*, *D*, $T_{frac,C}$ = $T_{frac,D}$ = 550 tons. The other parameters are the same as those in Figure 8. It can be observed from Figure 9a that the maximum momentary tension values of ropes *A*, *B* are T_{Amax} = 455 tons and T_{Bmax} = 444 tons. It can be seen from Figure 9b that the heaving displacement of platform 1, invertor 2, and pontoons 3 and 4 converge to near zero. The swaying displacement z_{1d} of the platform oscillates.

In Figure 10, the effect of larger hydrodynamic heaving damping coefficients on the transient response is demonstrated. In this case, the damping coefficients of all of the elements increased to be $C_{3,3} = 1.15 \times 10^6$ (N-s/m), $C_{4,4} = 2.96 \times 10^8$ (N-s/m), $C_{7,7} = C_{10,10} = 6 \times 10^4$ (N-s/m). The other parameters are the same as those in Figure 9. It was found that the swaying displacement z_{1d} of the platform significantly decreased. The mooring system therefore became more stable.

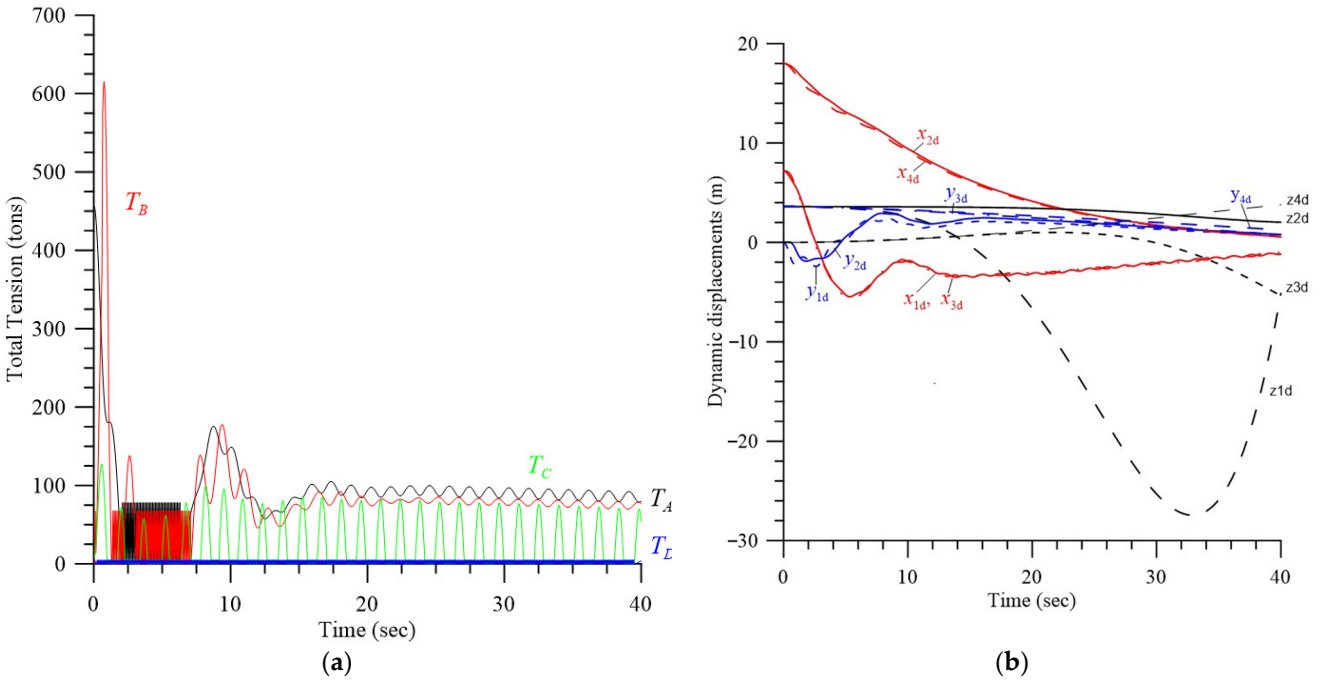

Figure 9. Transient response of mooring system with the double-rope parallel modes *B*, *C*, *D* (L_C = 100 m, L_D = 110 m, $T_{frac,A}$ = $T_{frac,B}$ = 750 tons, $T_{frac,C}$ = $T_{frac,D}$ = 550 tons). (**a**) Total tension of ropes. (**b**) Displacements of pontoons, turbine, and platform.

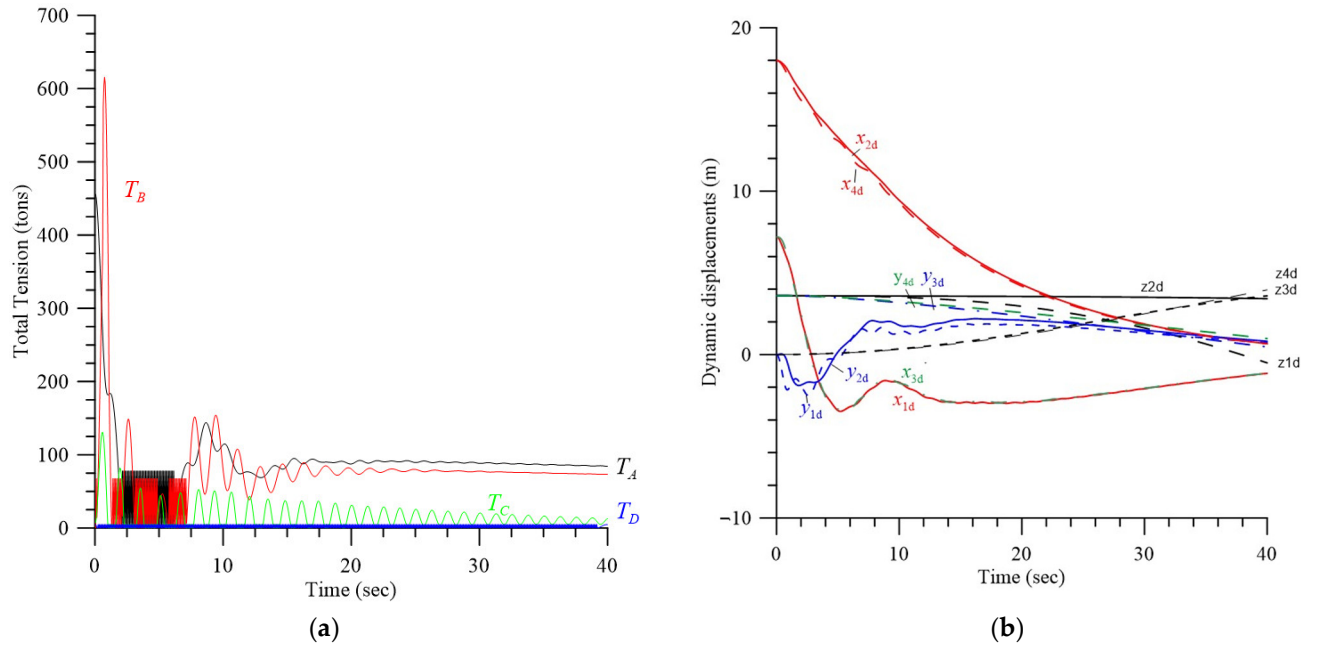

Figure 10. Transient response of mooring system with the double-rope parallel modes *B*, *C*, *D*, and larger heaving hydrodynamic damping. (**a**) Total tension of ropes. (**b**) Displacements of pontoons, turbine, and platform.

4.2.2. Transient Response and Improvement of Stability and Safety, L_C = 110 m, L_D = 100 m

In Figure 11, the effect of the lengths of ropes *C* and *D* on the transient response of the mooring system is depicted. Except for L_C = 110 m, L_D = 100 m, the other parameters are the same as those used in Figure 6. The effective spring constants K_{Ad} = 105.3 (tons/m), K_{Bd} = 631.3 (tons/m), K_{Cd} = 406.9(tons/m), K_{Dd} = 412.2 (tons/m).

The fracture strengths of ropes A, B, $T_{frac,A} = T_{frac,B} = 750$ tons. The fracture strengths of ropes C, D, $T_{frac,C} = T_{frac,D} = 162.5$ tons. It can be observed from Figure 8a that the tension of rope A is the greatest among ropes A, B, C, and D. The maximum momentary tensions of ropes A and B are T_{Amax} =461 tons and T_{Bmax} = 294 tons, respectively, which is significantly lower than the T_{Bmax} = 464 tons shown in Figure 6, with $L_C = L_D = 100$ m. It can be concluded that the effect of the lengths of ropes C and D on the maximum tensions of ropes A and B is significant. However, it is shown in Figure 8b that the heaving displacements of the invertor and pontoon 4 are significantly increased. Finally, the invertor is lifted to the water surface. The swaying displacement of the platform increases significantly. This means that the mooring system is unstable.

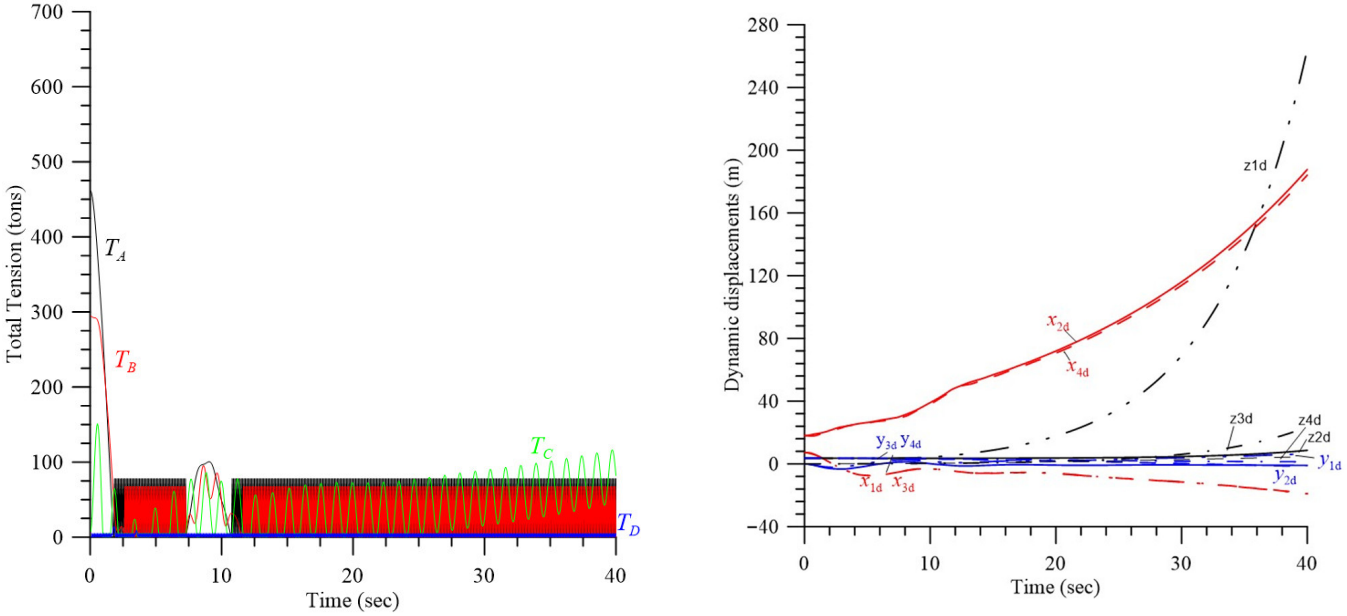

(**a**) (**b**)

Figure 11. Transient response of mooring system with $L_C = 110$ m, $L_D = 100$ m. (**a**) Total tension of ropes. (**b**) Displacements of pontoons, turbines, and platform.

In order to overcome the above disadvantages of the low fracture strength of the rope, the double-rope parallel mode was proposed. The effective spring constant of rope A K_{Ad} =105.3 (tons/m). The parameters of the integrated ropes B, C, and D are $K_{B,stage1} = \overline{K}_{Ba} = 205$ (tons/m), $T_{Bc} = 299$ tons, $K_{B,stage2} = 376.2$ (tons/m), $K_{C,stage1} = \overline{K}_{Ca} = 313.5$ (tons/m), $T_{Cc} = 137$ tons, $K_{C,stage2} = 940$ (tons/m), $K_{D,stage1} = \overline{K}_{Da} = 344.8$ (tons/m), $T_{Dc} = 136$ tons, $K_{D,stage2} = 1048$ (tons/m). The fracture strengths of ropes A, B, $T_{frac,A} = T_{frac,B} = 756$ tons. The fracture strengths of ropes C, D, $T_{frac,C} = T_{frac,D} = 550$ tons. The hydrodynamic heaving damping coefficients are increased as follows: $C_{3,3} = 1.15 \times 10^6$(N-s/m), $C_{4,4} = 2.96 \times 10^8$(N-s/m), $C_{7,7} = C_{10,10} = 6 \times 10^4$(N-s/m). The other parameters are the same as those in Figure 11. Figure 12a shows that the tensions of ropes are significantly decreased. Figure 12b demonstrates that the heaving displacements x_{2d}, x_{4d} are almost fixed. The swaying displacement z_{1d} of the platform is close to zero. This means that increasing the hydrodynamic damping is greatly helpful for the stability of the system.

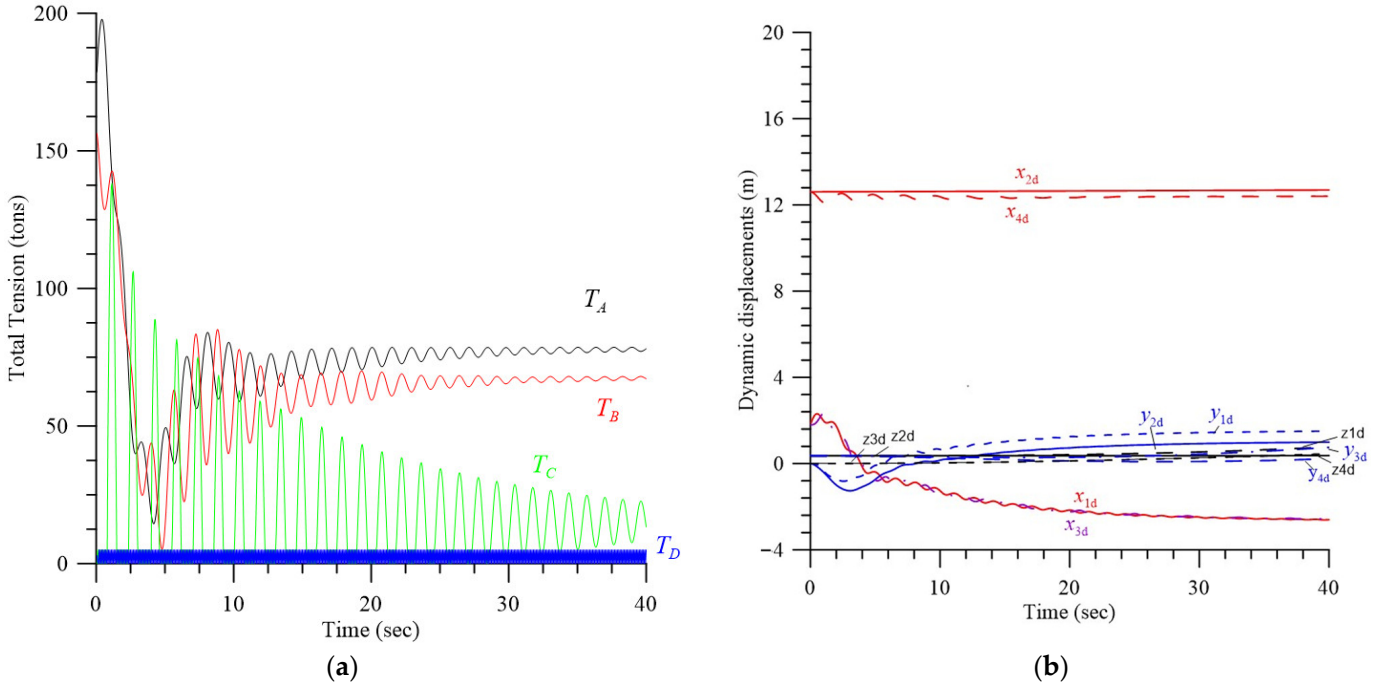

Figure 12. Transient response of mooring system with integrated rope and larger heaving damping. (**a**) Total tension of ropes. (**b**) Displacements of pontoons, turbine, and platform.

4.3. Effect of Initial Velocities

The new initial conditions are considered as follows:

$$\begin{aligned}\mathbf{Z}_d|_{t=0} &= \left[\begin{array}{cccccccccccccccccc} x_{1d0} & y_{1d0} & z_{1d0} & x_{2d0} & y_{2d0} & z_{2d0} & x_{3d0} & y_{3d0} & z_{3d0} & x_{4d0} & y_{4d0} & z_{4d0} & \varphi_{Tx0} & \varphi_{Ty0} & \varphi_{Tz0} & \varphi_{Px0} & \varphi_{Py0} & \varphi_{Pz0} \end{array}\right]^T \\ &= [0.05,\ 1.888, -0.003,\ 0.36,\ 1.884, -0.001,\ 0.36,\ 1.8,\ 0.36,\ 1.8,\ 0.36,\ 0, \cdots,\ 0]^T (\text{m; rad}),\end{aligned} \tag{32}$$

$$\begin{aligned}\dot{\mathbf{Z}}_d\Big|_{t=0} &= \left[\begin{array}{cccccccccccccccccc} \dot{x}_{1d0} & \dot{y}_{1d0} & \dot{z}_{1d0} & \dot{x}_{2d0} & \dot{y}_{2d0} & \dot{z}_{2d0} & \dot{x}_{3d0} & \dot{y}_{3d0} & \dot{z}_{3d0} & \dot{x}_{4d0} & \dot{y}_{4d0} & \dot{z}_{4d0} & \dot{\varphi}_{Tx0} & \dot{\varphi}_{Ty0} & \dot{\varphi}_{Tz0} & \dot{\varphi}_{Px0} & \dot{\varphi}_{Py0} & \dot{\varphi}_{Pz0} \end{array}\right]^T \\ &= \left[\begin{array}{cccccccc} 0.05(m/s), & 0, & 0, & 0.05(m/s), & 0, & \cdots, & 0 \end{array}\right]^T\end{aligned} \tag{33}$$

where the initial (angular) displacements are close to zero. The initial velocities in the x-direction of platform 1 and invertor 2 are 0.05 (m/s). The hydrodynamic heaving damping coefficients $C_{3,3} = 5756$ (N-s/m), $C_{4,4} = 1.465 \times 10^6$ (N-s/m), $C_{7,7} = C_{10,10} = 300$ (N-s/m), which is significantly lower than those in Figure 12. In Figure 13, the transient response with $L_C = L_D = 100$ m and the different initial conditions described the above cases are presented. The effective spring constant of rope A $K_{Ad} = 105.3$ (tons/m). The parameters of the integrated ropes B, C, and D are $K_{B,stage1} = \overline{K}_{Ba} = 205$ (tons/m), $T_{Bc} = 299$ tons, $K_{B,stage2} = 376.2$ (tons/m), $K_{j,stage1} = \overline{K}_{ja} = 344.8$ (tons/m), $T_{jc} = 136$ tons, $K_{j,stage2} = 1048$ (tons/m). $j = C, D$. The fracture strengths of ropes A, B, $T_{frac,A} = T_{frac,B} = 756$ tons. The fracture strengths of ropes C, D, $T_{frac,C} = T_{frac,D} = 550$ tons. The other parameters are the same as those employed in Figure 12. It can be seen from Figure 13a that the tensions are significantly lower than the fracture strengths. It is demonstrated in Figure 13b that the mooring system is stable.

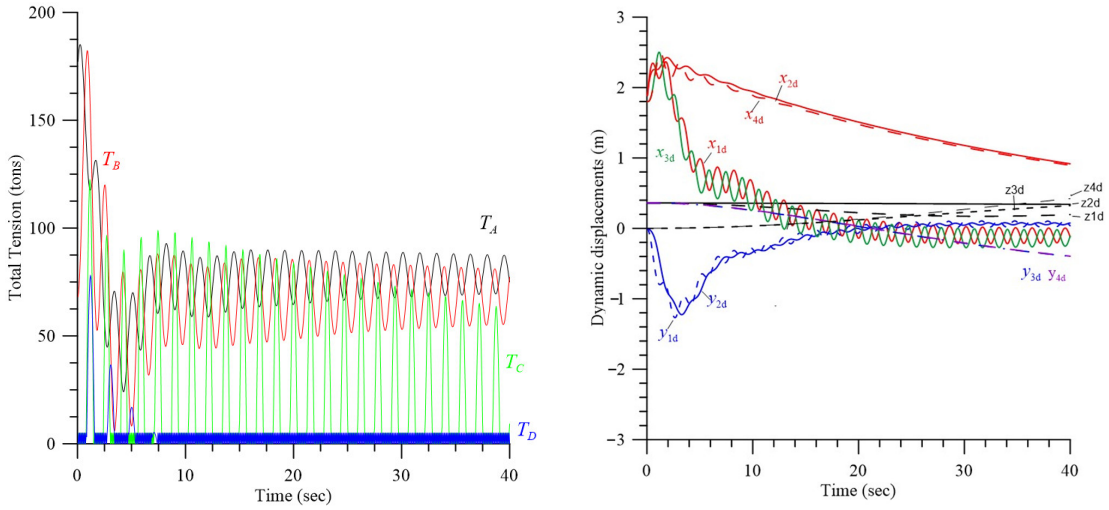

(**a**) (**b**)

Figure 13. Transient response of mooring system with different initial conditions. (**a**) Total tension of ropes. (**b**) Displacement of pontoons, turbines, and platform.

5. Conclusions

In this paper, the transient response of the transient translational-rotational motions of the mooring system was investigated for the ocean energy converter presented by Lin et al. [8] under a number of initial conditions. The normal power generation of the proposed turbine was 400 kW at a current velocity V = 1.6 m/s. Its maximum power coefficient of CP was 0.43. A semi-analytical method was presented for the system. The double-rope parallel mode was proposed. This mode was demonstrated to be able to effectively increase the buffering feature and fracture strength. The translational and rotational displacements of the mooring system will be significantly decreased with enough buffering features and hydrodynamic damping. Moreover, the effects of several parameters on the transient performance of the mooring system were investigated, and conclusions can be drawn as follows:

1. The lower the effective spring constants of the ropes are, the higher the buffering feature of the mooring system will be.
2. The higher the effective spring constants of the ropes are, the higher the momentary tension of the ropes will be.
3. In traditional setups, the lower the effective spring constants of single-rope mode are, the lower the fracture strength of the rope will be. This disadvantage can be overcome by using the double-rope parallel mode.
4. The effect of the lengths of ropes C and D on the transient response is significant.
5. The larger the hydrodynamic damping coefficients are, the stabler the mooring system will be.

Author Contributions: Conceptualization, S.-M.L. and W.-R.W.; methodology, S.-M.L.; software, S.-M.L.; H.Y.; validation, S.-M.L.; formal analysis, S.-M.L.; investigation, S.-M.L.; H.Y.; resources, S.-M.L. and W.-R.W.; data curation, H.Y.; writing—original draft preparation, S.-M.L.; writing—review and editing, W.-R.W.; visualization, S.-M.L.; supervision, S.-M.L.; funding acquisition, S.-M.L. and W.-R.W. All authors have read and agreed to the published version of the manuscript.

Funding: This work was financially supported by the Green Energy Technology Research Center from The Featured Areas Research Center Program within the framework of the Higher Education Sprout Project by the Ministry of Education (MOE) in Taiwan and the Ministry of Science and Technology of Taiwan, R. O. C. (NSTC 112-2218-E-110-008).

Institutional Review Board Statement: Not applicable.

Informed Consent Statement: Not applicable.

Data Availability Statement: The figures and the tables in this manuscript have clearly described all the data of this study.

Acknowledgments: The support of GETRC from The Featured Areas Research Center Program within the framework of the Higher Education Sprout Project by MOE in Taiwan and the Ministry of Science and Technology of Taiwan, R. O. C. (NSTC 112-2218-E-110-008) are gratefully acknowledged.

Conflicts of Interest: The authors declare no conflict of interest. The funders had no role in the design of the study; in the collection, analyses, or interpretation of data; in the writing of the manuscript, or in the decision to publish the results.

Nomenclature

A_{BX}: A_{BT}	cross-sectional area of surfaced cylinder of pontoons 3 and 4, respectively
A_{BY}, A_{TY}	damping area of platform and convertor under current, respectively
C	matrix of damping
C_{DFy}, C_{DTy}	damping coefficient of floating platform and convertor
E_i	Young's modulus of rope i, $i = A, B, C, D$
e_{frac}	fracture energy of rope
F_B	buoyance
f_{Pys}, f_{Tys}	the drag of the floating platform and the convertor under steady current
H_{bed}	depth of seabed
I_{Tj}, I_{Pj}	mass moment of inertia of the convertor and the platform about the j-axis.
g	gravity
K	matrix of stiffness
K_{id}	effective spring constant of rope i, $E_i A_i / L_i$
$L_{i,}$	length of rope i, $i = A, B, C, D$
$L_{E,}$	horizontal distance between the convertor and platform, $\sqrt{L_B^2 - (L_C - L_D)^2}$
M	matrix of mass
M_i	mass of element i
$M_{eff,i}$	effective mass of rope A in the i-direction
m_{ki}	hydrodynamic moment of convertor or platform about the i-axis
$\vec{R}$	coordinate
T_i	tension force of rope i
t	time variable
V	ocean current velocity
W_i	weight of component i
w_{PE}	weight per unit length of HSPE
x_i, y_i, z_i	displacements of component i
ε	strain
ρ	density of sea water
φ_{kj}	angular displacement of convertor or platform about the j-axis
θ_i	angles of rope i
δ_i	elongation of rope i
Subscript:	
0~4	mooring foundation, floating platform, convertor, and two pontoons, respectively
A, B, C, D	Ropes A, B, C, and D, respectively
crit	critical
$i\alpha$, $i\beta$	component α, β of rope $i = A, B, C$, and D
frac	fracture
s, d	static and dynamic, respectively
PE	PE dyneema rope
P	platform
T	convertor

Appendix A. Elements of the Mass Matrix M = $[M_{i,j}]_{18\times18}$

The translational inertia coefficients of platform 1:

$$M_{1,1} = \left(M_1 + M_{eff,x}\right),\ M_{1,j} = 0,\ j \neq 1; \qquad M_{2,2} = \left(M_1 + M_{eff,y}\right),\ M_{2,j} = 0,\ j \neq 2;$$

$$M_{3,3} = \left(M_1 + M_{eff,z}\right),\ M_{3,j} = 0,\ j \neq 3; \qquad M_{eff,x} = \frac{4\rho A L_A \sin\theta_A}{\pi^2},$$

$$M_{eff,y} = \frac{4\rho A L_A \cos\theta_A}{\pi^2}, \quad M_{eff,z} = 0$$

The translational inertia coefficients of invertor 2:

$$M4,4 = M2,\ M4,j = 0,\ j \neq 4;$$
$$M5,5 = M2,\ M5,j = 0,\ j \neq 5; \qquad M6,6 = M2,\ M6,j = 0,\ j \neq 6;$$

The translational inertia coefficients of pontoon 3:

$$M7,7 = M3,\ M7,j = 0,\ j \neq 7; \qquad M8,8 = M3, M8,j = 0,\ j \neq 8;$$
$$M9,9 = M3,\ M9,j = 0,\ j \neq 9;$$

The translational inertia coefficients of pontoon 4:

$$M10,10 = M4,\ M10,j = 0,\ j \neq 10;$$
$$M11,11 = M4,\ M11,j = 0,\ j \neq 11; \qquad M12,12 = M4,\ M12,j = 0,\ j \neq 12$$

The rotational inertia coefficients of invertor 2:

$$M13,13 = ITx,\ M13,j = 0,\ j \neq 13; \qquad M14,14 = ITy,\ M14,j = 0,\ j \neq 14;$$
$$M15,15 = ITz,\ M15,j = 0,\ j \neq 15;$$

The rotational inertia coefficients of platform 1:

$$M16,16 = IPx,\ M16,j = 0,\ j \neq 16; \qquad M17,17 = IPy,\ M17,j = 0,\ j \neq 17;$$
$$M18,18 = IPz,\ M18,j = 0,\ j \neq 18.$$

Appendix B. Elements of the Hydrodynamic Damping Matrix C = $[C_{i,j}]_{18\times18}$

The translational hydrodynamic damping coefficients of platform 1:

$$C_{1,1} = 5800(\text{N-s/m}), \quad C_{1,18} = 3.065\times10^4(\text{N-s}), \quad C_{1,j} = 0,\ j \neq 1,18;$$

$$C_{2,1} = 121.4(\text{N-s/m}), \quad C_{2,2} = 768.4(\text{N-s/m}) \quad C_{2,3} = 108.5(\text{N-s/m}),$$

$$C_{2,16} = 7.375\times10^4(\text{N-s}), \quad C_{2,18} = 7.374\times10^4(\text{N-s}) \quad C_{2,j} = 0,\ j \neq 1,2,3,16,18;$$

$$C_{3,3} = 5756(\text{N-s/m}) \quad C_{3,16} = -3.1174\times10^4(\text{N-s}), \quad C_{3,j} = 0,\ j \neq 3,16;$$

The translational hydrodynamic damping coefficients of invertor 2:

$$C_{4,4} = 1.465\times10^6(\text{N-s/m}), \quad C_{4,j} = 0,\ j \neq 4;$$

$$C_{5,4} = 2.085\times10^5(\text{N-s/m}), \quad C_{5,5} = 9.802\times10^5(\text{N-s/m}), \quad C_{5,6} = 1.256\times10^5(\text{N-s/m}), \quad C_{5,j} = 0,\ j \neq 4,5,6;$$

$$C_{6,6} = 7\times10^5(\text{N-s/m}), \quad C_{6,j} = 0,\ j \neq 6;$$

The rotational hydrodynamic damping coefficients of invertor 2:

$$C_{13,6} = -4.440\times10^6(\text{N-s}) \quad C_{13,13} = -\frac{\partial m_{Tx}}{\partial \dot{\varphi}_{2x}} = 13150(\text{N-m-s}), \quad C_{13,j} = 0,\ j \neq 6,13;$$

$$C_{14,14} = 2.837\times10^8(\text{N-m-s}), \quad C_{14,j} = 0,\ j \neq 14;$$

$$C_{15,4} = 7.453\times10^6(\text{N-s}), \quad C_{15,15} = 2.894\times10^7(\text{N-m-s}) \quad C_{15,j} = 0,\ j \neq 4,15;$$

The rotational hydrodynamic damping coefficients of platform 1:

$$C_{16,3} = 8.671\times10^4(\text{N-s}), \quad C_{16,16} = 1076(\text{N-m-s}), \quad C_{16,j} = 0,\ j \neq 3,16;$$

$$C_{18,1} = 8.654 \times 10^4 \text{(N-s)} \quad C_{18,18} = 5.951 \times 10^4 \text{(N-m-s)}, \quad C_{18,j} = 0,\ j \neq 1, 18;$$

Other coefficients:

$$C_{i,j} = 0,\ i = 7 \sim 12, 17;\ j = 1 \sim 18;$$

The above coefficients were presented by Lin et al. [8]. The hydrodynamic damping of pontoons 3 and 4 was neglected. In this study, for dynamic stability, the hydrodynamic heaving damping of pontoons 3 and 4 was considered as follows:

$C3,3 = 5756\ or\ 1.15 \times 106N - s/m$, $C4,4 = 1.465 \times 106\ or\ 2.93 \times 108N - s/m$,
$C7,7 = C10,10 = 300\ or\ 6 \times 104N - s/m$

Appendix C. Elements of the Stiffness Matrix K = $[K_{i,j}]_{18\times18}$

The translational stiffness coefficients of platform 1:

$$K_{1,1} = -\left(K_{Cd} + \frac{T_{As}\cos\theta_{As}}{L_A} + \frac{\sin\theta_{As}K_{Ad}x_{1s}}{L_A} - \frac{T_{Bs}\cos\theta_{Bs}}{L_B} - \sin\theta_{Bs}K_{Bd}\frac{(x_{2s}-x_{1s})}{L_B}\right)$$

$$K_{1,2} = -\left(\sin\theta_{As}K_{Ad}\frac{y_{1s}}{L_A} - \sin\theta_{Bs}K_{Bd}\frac{(y_{2s}-y_{1s})}{L_B}\right), \quad K_{1,4} = -\left(\frac{T_{Bs}\cos\theta_{Bs}}{L_B} - \sin\theta_{Bs}K_{Bd}\frac{(x_{2s}-x_{1s})}{L_B}\right)$$

$$K_{1,5} = -\sin\theta_{Bs}K_{Bd}\frac{(y_{2s}-y_{1s})}{L_B}, \quad K_{1,7} = K_{Cd},$$

$$K_{1,18} = 6508.5\text{N} \qquad K_{1j} = 0,\ j \neq 1, 2, 4, 5, 7, 18;$$

$$K_{2,1} = \left(K_{Ad}\frac{x_{1s}}{L_A}\cos\theta_{As} - K_{Bd}\frac{x_{1s}-x_{2s}}{L_B}\cos\theta_{Bs} - \left(\frac{T_{As}\sin\theta_{As}}{L_A} + \frac{T_{Bs}\sin\theta_{Bs}}{L_B}\right)\right)$$

$$K_{2,2} = \left(K_{Ad}\frac{y_{1s}}{L_A}\cos\theta_{As} - K_{Bd}\frac{y_{1s}-y_{2s}}{L_B}\cos\theta_{Bs}\right), \quad K_{2,4} = \left(K_{Bd}\frac{x_{1s}-x_{2s}}{L_B}\cos\theta_{Bs} + \frac{T_{Bs}\sin\theta_{Bs}}{L_B}\right),$$

$$K_{2,5} = K_{Bd}\frac{y_{1s}-y_{2s}}{L_B}\cos\theta_{Bs}, \qquad K_{2,16} = 2072\text{N},$$

$$K_{2,18} = 2043.5\text{N}, \qquad K_{2,j} = 0,\ j \neq 1, 2, 4, 5, 16, 18;$$

$$K_{3,3} = \left(\frac{T_{As}}{L_A} + \frac{T_{Bs}}{L_B} + \frac{T_{Cs}}{L_C}\right), \quad K_{3,6} = -\frac{T_{Bs}}{L_B}, \quad K_{3,9} = -\frac{T_{Cs}}{L_C}, \quad K_{3,16} = -6547\text{N}$$

$$K_{3,j} = 0,\ j \neq 3, 6, 9, 16;$$

The translational stiffness coefficients of invertor 2:

$$K_{4,1} = \left(\frac{T_{\text{Bs}}\cos\theta_{Bs}}{L_B} + \sin\theta_{Bs}K_{Bd}\frac{(x_{2s}-x_{1s})}{L_B}\right), \quad K_{4,2} = \sin\theta_{Bs}K_{Bd}\frac{(y_{2s}-y_{1s})}{L_B},$$

$$K_{4,4} = \left(K_{Dd} - \frac{T_{\text{Bs}}\cos\theta_{Bs}}{L_B} - \sin\theta_{Bs}K_{Bd}\frac{(x_{2s}-x_{1s})}{L_B}\right), \quad K_{4,5} = -\sin\theta_{Bs}K_{Bd}\frac{(y_{2s}-y_{1s})}{L_B}, K_{4,10} = -K_{Dd},$$

$$K_{4,15} = 1.5 \times 10^6\text{N} \qquad K_{4,j} = 0,\ j \neq 1, 2, 4, 5, 10, 15;$$

$$K_{5,1} = \left(K_{Bd}\frac{x_{1s}-x_{2s}}{L_B}\cos\theta_B\right),\ K_{5,2} = \left(K_{Bd}\frac{y_{1s}-y_{2s}}{L_B}\cos\theta_B\right),\ K_{5,4} = -\left(K_{Bd}\frac{x_{1s}-x_{2s}}{L_B}\cos\theta_B\right),$$

$$K_{5,5} = -\left(K_{Bd}\frac{y_{1s}-y_{2s}}{L_B}\cos\theta_B\right), \quad K_{5,13} = 2.349 \times 10^5\text{N}$$

$$K_{5,15} = 5.850 \times 10^5\text{N} \quad K_{5,j} = 0,\ j \neq 1, 2, 4, 5, 13, 15;$$

$$K_{6,3} = -\frac{T_{Bs}}{L_B}, \quad K_{6,6} = \left(\frac{T_{Bs}}{L_B} + \frac{T_{Ds}}{L_D}\right), \quad K_{6,12} = -\frac{T_{Ds}}{L_D},$$

$$K_{6,13} = -5.880 \times 10^5\text{N} \quad K_{6,j} = 0,\ j \neq 3, 6, 12, 13;$$

The translational stiffness coefficients of pontoon 3:

$$K_{7,1} = -K_{Cd}, \quad K_{7,7} = (K_{Cd} + A_{Bx}\rho g), \quad K_{7,j} = 0,\ j \neq 1,7;$$

$$K_{8,8} = \frac{T_{Cs}}{L_C}, \quad K_{8,2} = \frac{-T_{Cs}}{L_C}, \quad K_{8j} = 0,\ j \neq 2,8;$$

$$K_{9,3} = \frac{-T_{Cs}}{L_C}, \quad K_{9,9} = \frac{T_{Cs}}{L_C}, \quad K_{9,j} = 0,\ j \neq 3,9;$$

The translational stiffness coefficients of pontoon 4:

$$K_{10,4} = -K_{\mathrm{D}d}, \ K_{10,10} = (\ \ K_{\mathrm{D}d} + A_{B\mathrm{T}}\rho g), \quad K_{10,j} = 0,\ j \neq 4,10;$$

$$K_{11,5} = \frac{-T_{Ds}}{L_D}, \quad K_{11,11} = \frac{T_{Ds}}{L_D}, \quad K_{11,j} = 0,\ j \neq 5,11;$$

$$K_{12,6} = \frac{-T_{Ds}}{L_D}, \quad K_{12,12} = \frac{T_{Ds}}{L_D}, \quad K_{12,j} = 0,\ j \neq 6,12;$$

The rotational stiffness coefficients of invertor 2:

$$K_{13,3} = \frac{-T_{Bs}R_{TBx}}{L_B}, \quad K_{13,6} = \frac{T_{Bs}R_{TBx}}{L_B}, \quad K_{13,13} = \left(T_{Bs}\cos\theta_{Bs}R_{TBx} - \frac{\partial m_{Tx}}{\partial \varphi_{2x}}\right),$$

$$\frac{\partial m_{Tx}}{\partial \varphi_{2x}} = 4.866 \times 10^6(\text{N-m}), \quad K_{13,j} = 0,\ j \neq 3,6,13;$$

$$K_{14,6} = \frac{T_{Ds}R_{TDy}}{L_D}, \quad K_{14,12} = \frac{-T_{Ds}R_{TDy}}{L_D}, \quad K_{14,13} = -9.537 \times 10^5(\text{N-m})$$

$$K_{14,14} = T_{Ds}R_{TDy}, \quad K_{14,j} = 0,\ j \neq 6,12,13,14$$

$$K_{15,1} = \frac{-T_{Bs}R_{TBz}\cos\theta_B}{L_B}, \quad K_{15,4} = \frac{T_{Bs}R_{TBz}\cos\theta_B}{L_B}, \quad K_{15,13} = -5.022 \times 10^4(\text{N-m})$$

$$K_{15,15} = T_{Bs}R_{TBz}\cos\theta_B - \frac{\partial m_{Tz}}{\partial \varphi_{2z}}, \ \frac{\partial m_{Tz}}{\partial \varphi_{2z}} = 8.472 \times 10^6(\text{N-m}), \ K_{15,j} = 0,\ j \neq 1,4,13,15;$$

The rotational stiffness coefficients of platform 1:

$$K_{16,3} = \frac{T_{Bs}R_{PBx}}{L_B} - \frac{T_{As}R_{PAx}}{L_A}, \quad K_{16,6} = \frac{-T_{Bs}R_{PBx}}{L_B}, \quad K_{16,16} = T_{As}\cos\theta_{As}R_{PAx} + T_{Bs}\cos\theta_{Bs}R_{PBx} - \frac{\partial m_{Px}}{\partial \varphi_{1x}},$$

$$\frac{\partial m_{Px}}{\partial \varphi_{1x}} = 1.038 \times 10^5(\text{N-m}), \quad K_{16,j} = 0,\ j \neq 3,6,16;$$

$$K_{17,3} = \frac{T_{As}R_{PAy}}{L_A} + \frac{T_{Cs}R_{PCy}}{L_C}, \quad K_{17,9} = \frac{-T_{Cs}R_{PCy}}{L_C}, \quad K_{17,17} = T_{As}\cos\theta_{As}R_{PAy} + T_{Cs}R_{PCy}$$

$$K_{17,j} = 0,\ j \neq 3,9,17;$$

$$K_{18,1} = \frac{T_{As}\cos\theta_{As}R_{PAz}}{L_A} - \frac{T_{Bs}\cos\theta_{Bs}R_{PBz}}{L_B}, \ K_{18,2} = \frac{-T_{Cs}R_{PCz}}{L_C}, \ K_{18,4} = \frac{T_{Bs}\cos\theta_{Bs}R_{PBz}}{L_B},$$

$$K_{18,5} = \frac{T_{Cs}R_{PBz}}{L_C}, \quad K_{18,18} = T_{As}\cos\theta_{As}R_{PAz} + T_{Bs}\cos\theta_{Bs}R_{PBz} + T_{Cs}R_{PCz} - \frac{\partial m_{Pz}}{\partial \varphi_{1z}},$$

$$\frac{\partial m_{Pz}}{\partial \varphi_{1z}} = 1.010 \times 10^5(\text{N-m}), \quad K_{18,j} = 0,\ j \neq 1,2,4,5,18$$

References

1. Chen, Y.Y.; Hsu, H.C.; Bai, C.Y.; Yang, Y.; Lee, C.W.; Cheng, H.K.; Shyue, S.W.; Li, M.S. Evaluation of test platform in the open sea and mounting test of KW Kuroshio power-generating pilot facilities. In Proceedings of the 2016 Taiwan Wind Energy Conference, Keelung, Taiwan, 24–25 November 2016.
2. IHI; NEDO. The Demonstrtion Experiment of the IHI Ocean Current Turbine Located Off the Coast of Kuchinoshima Island, Kagoshima Prefecture, Japan, 14 August 2017. Available online: https://tethys.pnnl.gov/project-sites/ihi-ocean-current-turbine (accessed on 28 August 2021).
3. Nobel, D.R.; O'Shea, M.; Judge, F.; Robles, E.; Martinez, R.F.; Thies, P.R.; Johanning, L.; Corlay, R.; Davey, T.A.D.; Vejayan, N.; et al. Standardising Marine Renewable Energy Testing: Gap Analysis and Recommendations for Development of Standards. *J. Mar. Sci. Eng.* **2021**, *9*, 971. [CrossRef]
4. Lin, S.M.; Chen, Y.Y.; Hsu, H.C.; Li, M.S. Dynamic Stability of an Ocean Current Turbine System. *J. Mar. Sci. Eng.* **2020**, *8*, 687. [CrossRef]
5. Lin, S.M.; Chen, Y.Y. Dynamic stability and protection design of a submarined floater platform avoiding Typhoon wave impact. *J. Mar. Sci. Eng.* **2021**, *9*, 977. [CrossRef]
6. Lin, S.M.; Chen, Y.Y.; Liauh, C.T. Dynamic stability of the coupled pontoon-ocean turbine-floater platform-rope system under harmonic wave excitation and steady ocean current. *J. Mar. Sci. Eng.* **2021**, *9*, 1425. [CrossRef]
7. Lin, S.M.; Liauh, C.T.; Utama, D.W. Design and dynamic stability analysis of a submersible ocean current generator-platform mooring system under typhoon irregular wave. *J. Mar. Sci. Eng.* **2022**, *10*, 538. [CrossRef]
8. Lin, S.M.; Utama, D.W.; Liauh, C.T. Coupled translational-rotational stability analysis of a submersible ocean current converter-platform mooring system under typhoon wave. *J. Mar. Sci. Eng.* **2023**, *11*, 518. [CrossRef]
9. Anagnostopoulos, S.A. Dynamic response of offshore platforms to extreme waves including fluid-structure interaction. *Eng. Struct.* **1982**, *4*, 179–185. [CrossRef]
10. Geuzaine, P.; Farhat, C.; Brown, G. Application of a three-field nonlinear fluid-structure formulation to the prediction of the aeroelastic parameters of an f-16 fighter. *Comput. Fluids* **2003**, *32*, 3–29.
11. Bathe, K.J.; Nitikitpaiboon, C.; Wang, X. A mixed discplacement-based finite element formulation for acoustic fluid-structure interaction. *Comput. Struct.* **1995**, *56*, 225–237. [CrossRef]
12. Lin, S.M.; Lee, S.Y.; Tsai, C.C.; Chen, C.W.; Wang, W.R.; Lee, J.F. Wave modes of an elastic tube conveying blood. *CMES Comput. Model. Eng. Sci.* **2008**, *34*, 33–54.
13. Lin, S.M.; Wang, W.R.; Lee, S.Y.; Chen, C.W.; Hsiao, Y.C.; Teng, M.J. Wave modes of a pre-stressed thick tube conveying blood on the viscoelastic foundation. *Appl. Math. Model.* **2015**, *39*, 466–482. [CrossRef]
14. Belibassakis, K.A. A boundary element method for the hydrodynamic analysis of floating bodies in variable bathymetry regions. *Eng. Anal. Bound. Elem.* **2008**, *32*, 796–810. [CrossRef]
15. Tsui, Y.Y.; Huang, Y.C.; Huang, C.L.; Lin, S.W. A finite-volume-based approach for dynamic fluid-structure interaction. *Numer. Heat Transf. Part B Fundam.* **2013**, *64*, 326–349. [CrossRef]
16. Hasanpour, A.; Istrati, D.; Buckle, I. Coupled SPH–FEM Modeling of Tsunami-Borne Large Debris Flow and Impact on Coastal Structures. *J. Mar. Sci. Eng.* **2021**, *9*, 1068. [CrossRef]